Carbon/Metal Oxide Composites and Their Application in Lithium-Ion Batteries

by

Yue Cai

Department of Chemistry
Duke University

Date:_____

Approved:

_____
Jie Liu, Supervisor

_____
Chakrapani Varanasi

_____
Benjamin Wiley

Thesis submitted in partial fulfillment of
the requirements for the degree of
Master of Science in the Department of
Chemistry in the Graduate School
of Duke University

2013

ABSTRACT

Carbon/Metal Oxide Composites and Their Application in Lithium-Ion Batteries

by

Yue Cai

Department of Chemistry
Duke University

Date:_____

Approved:

_____
Jie Liu, Supervisor

_____
Chakrapani Varanasi

_____
Benjamin Wiley

An abstract of a thesis submitted in partial fulfillment of the requirements for the degree of Master of Science in the Department of Chemistry in the Graduate School of Duke University

2013

Copyright by
Yue Cai
2013

Abstract

The first chapter introduces the background about energy storage and lithium ion battery. The concepts of graphene, carbon nanotube, and carbon aerogel were covered as well. Then powder-based metal oxide-carbon composite materials and binder-free CNT-metal oxide films for lithium storage applications were further elaborated. Finally, the significance of our research was summarized.

The second chapter is about freestanding and highly conductive Fe_3O_4/Graphene/CNT film as lithium-ion battery anodes. Iron oxide is intensively studied as a lithium-ion battery anode material due to its high theoretical specific capacity, but it has low conductivity and poor cycling performance. Herein, we present the design of freestanding Fe_3O_4/graphene/Carbon nanotube film via in-situ growth by solvothermal reaction, vacuum filtration and annealing methods. The film had a sheet resistance of 23 Ω/□ and a BET surface area of 132 m^2/g. The synergistic effect of graphene and CNTs provide a flexible matrix to accommodate the volume change of metal oxide in lithium ion batteries application. This lightweight film was tested without using a current collector, binder and conducting additives, eliminating unnecessary weight in the overall devices. The film shows excellent cyclic performances, and stable rate capability. The specific capacity retained 803 mAh/g at the rate of 200 mA/g after 50 cycles. This method demonstrated a promising path for flexible energy storage devices.

The third chapter discusses facile synthesis of three-dimensional TiO_2/carbon co-aerogel nanostructures and their applications for energy storage. In the field of energy storage, it is important to design new materials and understand the fundamental principles of the electrode structure. Facile synthesis of TiO_2/carbon co-aerogel material via a sol-gel method was discussed. This new material was composed of a 3-D interconnected network of TiO_2 and carbon aerogel. TEM, SEM, XRD, BET SA, and electrochemistry measurements were discussed. With an operating voltage between 0.05 and 3.00 V, the discharge capacity was ~400 mAh/g at 168 mA/g current density.

Dedication

I dedicate this thesis to my family for their love and support.

Contents

Abstract iv

List of Tables ix

List of Figures x

Acknowledgements xv

1. Introduction 1

1.1 Energy storage and lithium ion battery 1

1.1.1 Structure of LIB 5

1.1.2 Alternative LIB anode materials and iron oxides 8

1.2 Graphene 15

1.3 Carbon nanotubes 19

1.4 Carbon aerogel 22

1.5 Metal oxide-carbon composites 25

1.6 Binder-free CNT-iron oxide films 31

1.7 Significance of our research 35

2. Free-standing and Highly Conductive Fe_3O_4/Graphene/CNT Film as Lithium-Ion Battery Anodes 36

2.1 Introduction 36

2.2 Experimental section 38

2.2.1 Preparation of graphene oxide 38

2.2.2 Preparation of Fe_3O_4/graphene 39

2.2.3 Preparation of CNTs 39

2.2.4 Preparation of Fe_3O_4/ graphene/ CNTs film 40

2.2.5 Preparation of commercial Fe_3O_4 electrode 40

2.2.6 Characterization 40

2.3 Results and discussion 41

2.4 Conclusions 60

3. Facile Synthesis of Three-dimensional Metal Oxide/Carbon co-Aerogel Nanostructures and Their Application for Energy Storage 61

3.1 Introduction 61

3.2 Experimental sections 63

3.2.1 Carbon aerogel synthesis 63

3.2.2 C/TiO_2 co-aerogel aerogel synthesis 63

3.2.2.1 Preparation of resorcinol-formaldehyde (RF) sol precursor 63

3.2.2.2 Preparation of TiO_2 (Ti) sol precursor 64

3.2.3 Preparation of LIB electrodes 64

3.3 Results and discussion 65

3.4 Conclusions 71

Appendix A 73

References 75

List of Tables

Table 1: Theoretical specific capacities and principal reactions of LIB anode materials.[12]13

Table 2: Film with different CNT content, and their specific capacities at current density of 200 mA/g. 43

Table 3: Film with different carbon weight percentage, and their specific capacities at current density of 200 mA/g. 47

List of Figures

Figure 1: US Energy Consumption by Source. Source: US Energy Information Administration 2

Figure 2: US carbon dioxide emission. Source: US EPA Government. 2

Figure 3: Representative applications for rechargeable batteries.[2] 4

Figure 4: The comparison of specific power and specific energy of energy-storage devices known as a Ragone plot.[6] 5

Figure 5: Typical commercial Li–ion battery showcasing the charge/discharge intercalation mechanism.[9] 6

Figure 6: Schematic of laptop's battery: Powder composites where the active material is blended with carbon powder to improve electron mobility through the composite structure.[6] 7

Figure 7: A schematic representation of the different reaction mechanisms observed in electrode materials for lithium batteries. Black circles: voids in the crystal structure, blue circles: metal, yellow circles: lithium.[8] 9

Figure 8: Specific capacities and capacity densities for selected alloying reactions. Values for graphite are given as a reference.[8] 9

Figure 9: Schematic of morphological changes that occur in Si during electrochemical cycling.[10] 10

Figure 10: (a) SEM images and (b)TEM images of as-prepared anatase TiO_2 nanosheets hierarchical spheres.[14] 12

Figure 11: Upper left pictures show an iron oxide dust storm that swept over Sydney and iron oxides precipitating from the Rio Tinto water in Spain. The rest pictures shows the magnetite Fe_3O_4 and its crystal structure.[17] 14

Figure 12: Graphene is a 2D building material for carbon materials of all other dimensionalities. It can be wrapped up into 0D buckyballs, rolled into 1D nanotubes or stacked into 3D graphite.[24] 16

Figure 13: Scanning electron micrograph (SEM) of a relatively large graphene sheet. Most of the crystal's faces are zigzag and armchair edges as indicated by blue and red lines in the inset.[24] 16

Figure 14: Schematic model of a graphene oxide sheet and graphene.[27] 18

Figure 15: Scheme showing the chemical route to the synthesis of aqueous graphene dispersions. (1) Oxidation of graphite (black blocks) to graphite oxide (lighter coloured blocks) with greater interlayer distance. (2) Exfoliation of graphite oxide to obtain GO colloids that are stabilized by electrostatic repulsion. (3) Controlled conversion of GO to conducting graphene colloids through deoxygenation by hydrazine reduction.[28] 18

Figure 16: A 10-μm-thick chemically converted graphene film prepared by vacuum filtration. The film exhibits a shiny metallic luster. A strip (top inset) cut from the film is bent to demonstrate its flexibility.[28] 19

Figure 17: CNTs consisting of (a) 5 graphene sheets, (b) 2 graphene sheets, and (3) 7 graphene sheets.[43] 20

Figure 18: Energy-related applications of CNTs. (A) Mixture of MWNTs and active powder for battery electrode. (B) Concept for supercapacitors based on CNT forests. (C) Solar cell using a SWNT-based transparent conductor. (D) Prototype portable water filter using a functionalized tangled CNT mesh in the latest stage of development.[45] 21

Figure 19: Digital photographs: (a) 180° folded functionalized FWNT thin film (b) functionalized FWNT thin film carbonized at 600 °C for 2 h. 22

Figure 20: Reaction of resorcinol with formaldehyde under basic conditions.[57] 23

Figure 21: Model of gelation progress with (a) high and (b) low catalyst to water (C/W) ratios.[58] 24

Figure 22: Synthetic scheme showing the versatility associated with carbon aerogel synthesis.[59] 24

Figure 23: Electrolyte-infiltrated electrode structures incorporating electron paths, active, and inactive materials, using composites, versus a nanoarchitecture incorporating electron paths wired to the active material.[62] 25

Figure 24: Schematic of a flexible structure of GNSs and Fe_3O_4 particles.[36] 26

Figure 25: (a) SEM image of the as-synthesized hematite spindles. (b) SEM image of the carbon precursor coated hematite spindles. (c) SEM image of the carbon coated Fe_3O_4 spindles (Fe_3O_4–C composites). (d) High resolution TEM image of the Fe_3O_4–C composites. The insets are close views of corresponding samples, all unmarked scale bars are 50 nm.[63] 27

Figure 26: (a) Schematic illustration of the formation of the yolk–shell Fe_3O_4@C composite. (b) TEM images of the Fe_3O_4@C composite.[64] 27

Figure 27: Schematic illustration of synthesis of 2D core-shell G@MO@C hybrids: (a) hydrolysis of metal salt on GO; (b) in-situ polymerization of PF on G@MO; (c) carbonization of PF.[65] 28

Figure 28: (a) SEM image and (b, c) TEM images of TiO_2-nanosheets[66] 29

Figure 29: Schematic illustration of three basic nanostructures to alleviate the pulverization problem in SnO_2 anode materials: (a) hollow structures (b) 2D nanosheets, and (c) amorphous carbon coating.[68] 30

Figure 30: Scheme illustrates the formation of the Fe_3O_4/carbon microspheres.[70] 31

Figure 31: Schematic of the synthesis procedure and the structure of an Fe_2O_3/SWCNT membrane. Photograph showing the flexible membrane obtained after oxidation.[71] 32

Figure 32: (a) SEM images of the nanostructured Fe_3O_4 electrode surface. (b) Comparison of specific capacity versus cycle number for various Fe_3O_4 electrodes at C rate: nano, micro1, and micro2. [72] 33

Figure 33: (a) High magnification TEM images for the precycle Fe_3O_4−CNT composite anode. (b) A photograph of the Cu cylinder wrapped with CNTs after sputtering. (c) Rate capability of Fe_3O_4−CNT. Values based on the Fe_3O_4 mass and the total anode mass are in black and red colors, respectively.[73] 34

Figure 34: Schematic illustration of the fabricated flexible and conductive film using graphene/ MnO_2/CNTs.[74] 34

Figure 35: Structure of the Fe_3O_4/graphene/CNT film. 41

Figure 36: (a) The Fe_3O_4/graphene film cracks without CNT after filtration. (b and c) The flexible Fe_3O_4/graphene/CNT film peeled off from filtration membrane. 45

Figure 37: Cyclic performance of Fe_3O_4/graphene/CNT film with different carbon weight percentage at current density of 200 mA/g. Film A, B and C has total carbon content of 10, 30, and 57 % wt. respectively. 48

Figure 38: XRD patterns of Fe_3O_4/graphene/CNTs film annealed at (a) 500 °C and (b) 600 °C in Ar atmosphere for 4 hours. 50

Figure 39: Stress-strain curve of the flexible Fe_3O_4/graphene/CNTs film after annealing treatment at 600 °C. 51

Figure 40: TEM images of (a) carbon nanotubes, (b) Fe_3O_4 nanoparticles grown on graphene sheets, (c) annealed Fe_3O_4/graphene/CNTs film re-dispersed via sonification, (d) SEM image of a fractured annealed Fe_3O_4/graphene/CNTs film highlighting the interconnected CNTs network. 53

Figure 41: Illustration for binder-free coin cell structure. 54

Figure 42: The charge and discharge curves of the Fe_3O_4/graphene/CNT film annealed at 500 °C for 1st, 2nd, and 3rd cycle at 200 mA/g. 55

Figure 43: The charge and discharge curves of the Fe_3O_4/graphene/CNT film annealed at 600 °C for 1st, 2nd, 5th and 10th cycle at 200 mA/g. 56

Figure 44: The charge and discharge curves of commercial Fe_3O_4 for 1st, 2nd, 5th and 10th cycle at 200 mA/g. 57

Figure 45: (a) Cyclic performance of Fe_3O_4/graphene/CNT film (red square) and commercial Fe_3O_4 (blue triangle) at 200 mA/g. (b) Rate capability of Fe_3O_4/graphene/CNTs film (red square) in comparison to commercial Fe_3O_4 (blue triangle). 58

Figure 46: Optical photos showing a mixture of TiO_2 and RF sol (a), TiO_2/RF organic co-aerogel after 5-day aging under 72 °C in oven (b), solvent exchange in acetone(c), and TiO_2/carbon co-aerogel monolith after 4-hour pyrolysis under 900 °C in nitrogen atmosphere (d). 65

Figure 47: Optical photo showing organic RF aerogel before and after critical point drying. 67

Figure 48: Optical images showing a piece of TiO_2/carbon co-aerogel monolith (a), TiO_2 aerogel after removing carbon component by air oxidation at 500°C for 5 hours (b),

carbon aerogel after removing TiO_2 component by HF treatment for 24 hours(c), and respective SEM pictures (d-f). The proposed co-aerogel structure scheme (g). SEM images contributed by our previous group memeber Dr. Sungwoo-Yang. 68

Figure 49: High magnification TEM images showing TiO_2 nanocrystals well mixed in carbon matrix (a,b), the blue arrows marked the carbon layers, and the red circles marked the TiO_2 particles. XRD patterns of anatase phase TiO_2 in the co-aerogel (c). BET surface area of TiO_2-carbon co-aerogel samples with different TiO_2 ratio (d). TEM images contributed by our collaborator Dr. Haiyan Wang. 68

Figure 50: The 1^{st} and 10^{th} galvanostatic charge and discharge curves of the TiO_2/carbon co-aerogel (a) and reference carbon aerogel (b) at a rate of 1C (= 168 mA/g) in 0.05-3.0 V vs. Li^+/Li window. Scan rate performance (from 1C to 50C, then back to 1C) for co-aerogel in comparison to carbon aerogel (c). The 1^{st} and 10^{th} galvanostatic charge and discharge curves of the TiO_2/carbon co-aerogel (d) in 1.0-3.0 V vs. Li^+/Li window. 70

Acknowledgements

First, I would like to thank my advisor Dr. Jie Liu for providing me the opportunity to conduct research, and teach me the importance of independent thinking, hard working, and staying strong. I would also like to thank all the members in Liu group for supporting me both academically and personally.

In addition, I would like to thank Dr. Chakrapani Varanasi for teaching me academic writing and presenting skills, and funding support from Army Research Office. This work is in part supported by a research grant from Army Research Office (ARO) under Contract W911NF-04-D-0001. I thank Dr. Benjamin Wiley for encouragement during the past three years.

Special thanks for our group member Dr. Sungwoo Yang (Harry) for collaboration. In the co-aerogel work, Dr. Sungwoo Yang (Harry) took the SEM pictures and collected the LIB electrochemistry data. Dr. Haiyan Wang and Joon Hwan Lee took the high-resolution TEM images of the TiO_2/C co-aerogel samples from Texas A&M University, department of electrical engineering.

Most importantly, thanks to my husband Dr. Pan Wu. Your excellent understanding toward graduate school life is really important to me.

Special thanks to my parents for trusting me, and staying open-minded to every decision I made during these years.

1. Introduction

1.1 Energy storage and lithium ion battery

Traditional fossil fuels are finite energy resources. According to data from US Energy Information Administration, about 84% of our energy supply relies on fossil fuels. Specifically, 38% energy supply is from petroleum, 25% from natural gas, and 21% from coal (Figure 1). It is estimated that the coal reserve can provide more than 100 years for human beings. Moreover, the awareness has also been raised in global warming effect and climate change. Human activities also have a significant impact on the environment. For instance, the CO_2 is a primary green house gas emitted from the combustion of fossil fuel resources. Figure 2 shows the US CO_2 emission mainly from converting fossil fuel to electricity (38%), and combustion of gasoline and diesel in transportation (31%). Fossil fuels are finite sources and their waste emissions have negative effect on the environment. It is important to develop alternative renewable energy. Renewable energy refers to solar, wind, biomass, geothermal, and hydropower energy, to name just a few. They are clean, emission-free, and abundant in nature. However, these energy resources are intermittent and unevenly distributed on the earth, which means they are not continuously available during the whole day. As a result, energy storage is essential for the sustainable future.

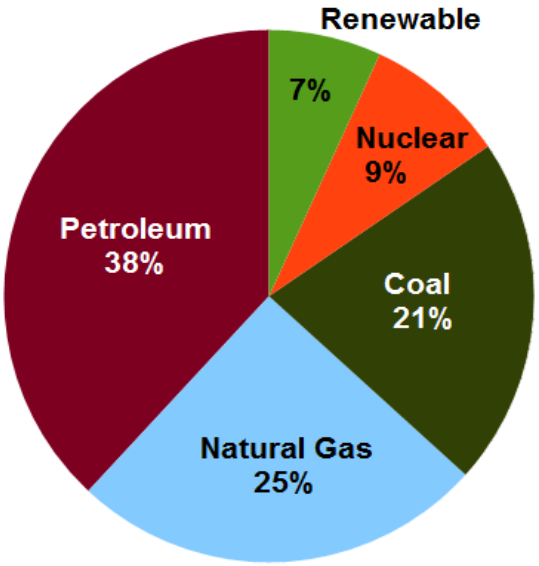

Figure 1: US Energy Consumption by Source. Source: US Energy Information Administration

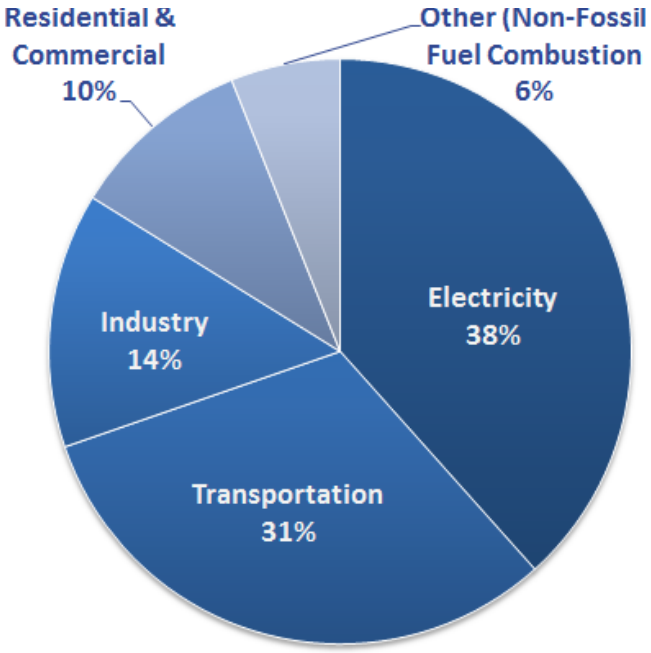

Figure 2: US carbon dioxide emission. Source: US EPA Government.

Energy storage is essential for future renewable energy applications. In the past decade, there are numerous research aimed to meet the ever-increasing demand for renewable energy resources and energy storage devices. Generally, batteries, electrochemical capacitors (ECs), and fuel cells are the three main electrochemical systems used in energy storage. Compared to EC and fuel cells, batteries have gained the established market position so far.[1] Among batteries, rechargeable batteries are the most successful technologies that can repeatedly generate electricity from stored materials via electrochemical reactions (Figure 3).[2] Obviously, lithium ion batteries (LIBs) are the most popular rechargeable batteries. LIBs store 1-3 times more energy per unit weight and volume than lead-acid or Ni-Cd batteries.[3] Figure 4 shows LIBs have high specific energy (150–200 W h/kg, here specific energy refers to how far a car can go on a single charge, while specific power refers how fast a car can go on a single charge), and they are widely used in portable electronic devices, such as cell phones and laptops. LIB is also promising candidate for next-generation electric vehicles. For example, Tesla Roadster is an electric vehicle powered by LIBs.

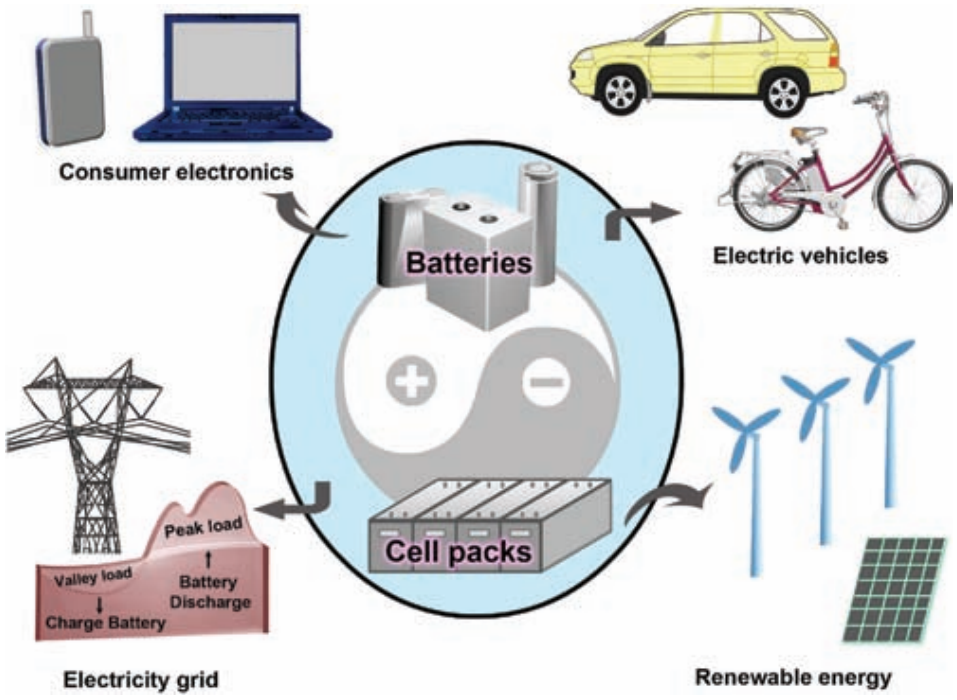

Figure 3: Representative applications for rechargeable batteries.[2]

In spite of the current progress in the fields of LIBs, the challenges for LIBs still remain in aspects of improving specific energy and power (Figure 4), fast charging process, stable cyclic stability, long service time, and safety issues. [4-6] For instance, the Apple MacBook's battery is designed to deliver up to 1000 full charge and discharge cycles before it reaches 80 percent of its original capacity. To reach these goals, high specific capacity, wide cell voltage windows, and highly reversible reactions even after repeated of charge/discharge cycles are essential requirements.[7]

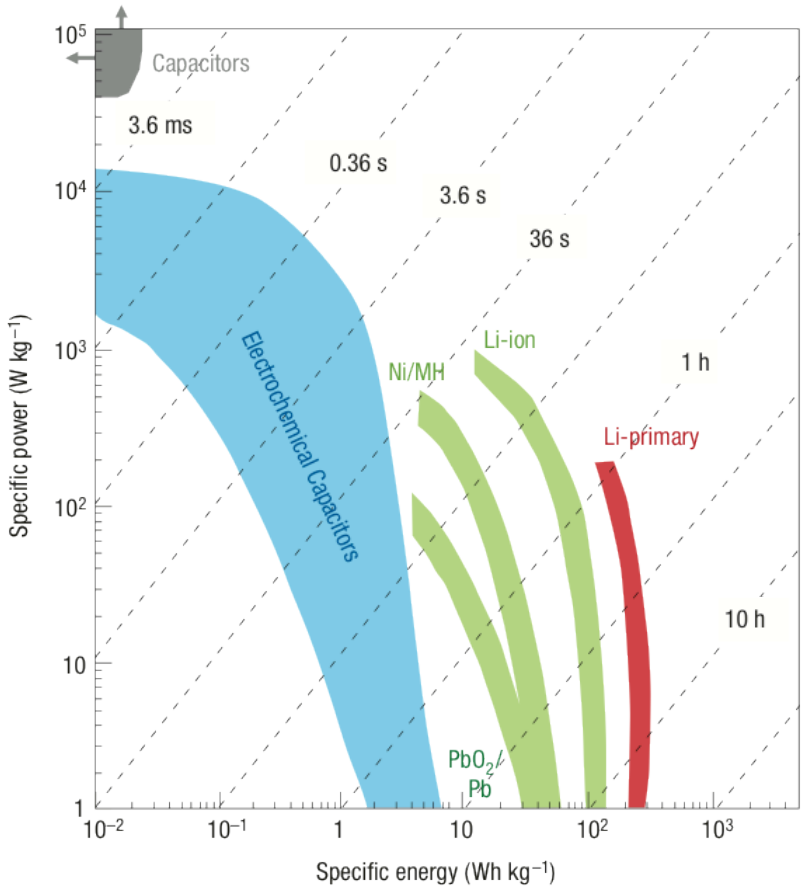

Figure 4: The comparison of specific power and specific energy of energy-storage devices known as a Ragone plot.[6]

1.1.1 Structure of LIB

In 1991, Sony released the first commercial lithium ion battery. The commercial LIB is composed of lithium-cobalt oxide ($LiCoO_2$) cathode, a porous electrically insulating separator, organic electrolyte containing lithium hexafluorophosphate ($LiPF_6$) salt with ethylene carbonate-organic solvent mixture, and graphite anode, as illustrated in Figure 5. The structure of the $LiCoO_2$ can be considered as a cubic close packed array of oxide ions with Co (III), while lithium ions occupy the octahedral voids in alternate

sheets.[8] Upon charging process, the lithium ions are extracted from the $LiCoO_2$ cathode, migrated through the electrolyte, and inserted into the graphite layers in the anode.

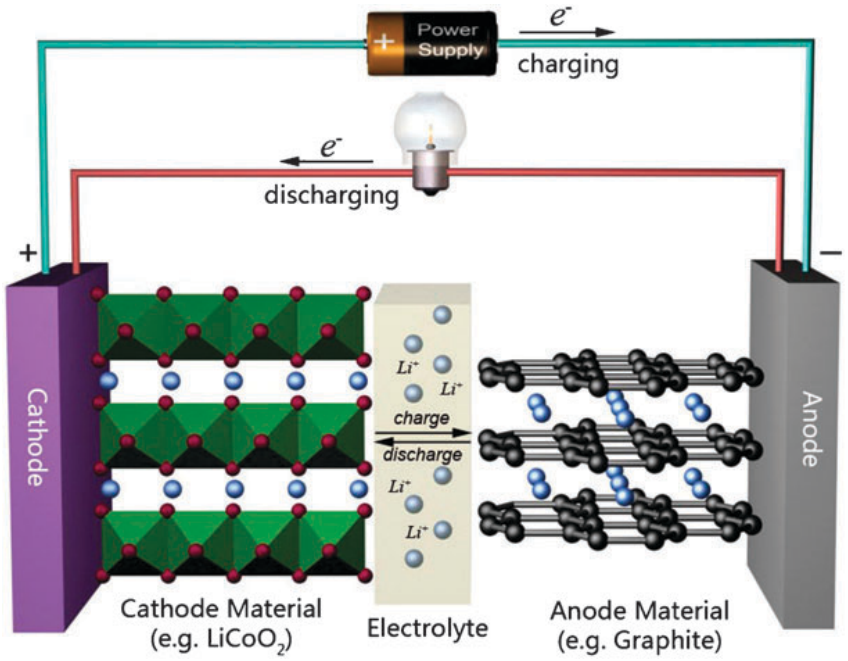

Figure 5: Typical commercial Li–ion battery showcasing the charge/discharge intercalation mechanism.[9]

Conventional approach to make LIB anode electrode is described as 'slurry-cast' method. Briefly, the paste is composed of electrochemically-active material, binder, and conductive additives, according to the weight ratio of 8:1:1. Then the organic solvent (e.g N-Methyl-2-pyrrolidone, NMP) is added into the mortar to dissolve the binder (e.g. Polyvinylidene fluoride, PVDF). Then active material together with conductive additives (e.g. carbon black) is added into the glue and mixed well. Finally, the glue-like paste is casted on Cu foil current collector. This metal foil is heated in a 70 °C oven to remove the

liquid solvent before transferring to overnight vacuum-dried oven at 120 °C to completely remove the organic solvent.

The above-mentioned 'slurry-cast' method has its own limitations. First, there are several components give extra weight in the electrode, such as Cu foil current collector, the PVDF binder, and conductive carbon additives. Moreover, their contribution to specific capacity is negligible. Second, the electrode structure design is simple, and the electron pathway connected by carbon black particles may not be efficient (Figure 6). Failure of the electrical contact happens during the charging-discharging process, and the amount of active material in the electrochemical reaction is reduced. As a result, the capacity fades quickly upon repeated cycles.

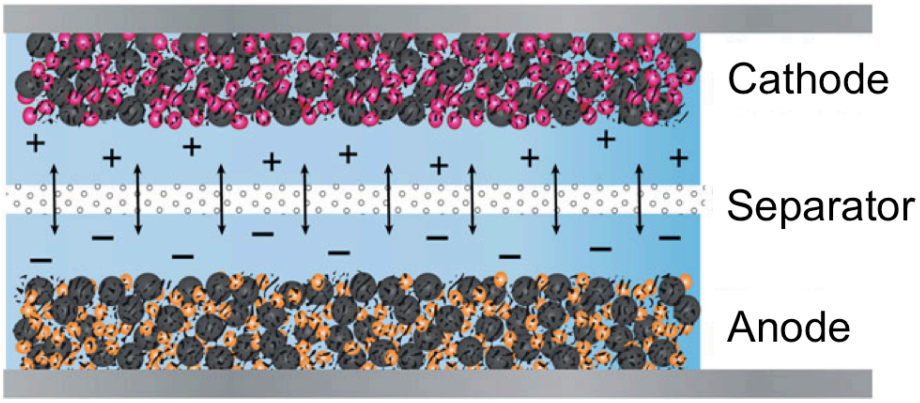

Figure 6: Schematic of laptop's battery: Powder composites where the active material is blended with carbon powder to improve electron mobility through the composite structure.[6]

In LIBs, electrode material is an important component. The reason is that the battery's overall performances, specific capacity, cost and safety all depend on the electrode material. Our work focuses on the study of LIB anode material, because there

are a lot of challenges to improve current commercialized graphite based anode material. Graphite has a theoretical specific capacity of 372 mAh/g for the end compound LiC_6, which is relatively low compared with other anode material candidates. Furthermore, graphite material performance is not stable and specific capacity decreases quickly especially at high current density, which is not desirable to meet future requirements in various applications.

1.1.2 Alternative LIB anode materials and iron oxides

In addition to the above mentioned graphite anode material, several alternative anode materials have been studied as well. As summarized in Figure 7, anode materials can be further categorized into three lithium ion reaction mechanisms. The first type is lithium insertion reaction. Graphite belongs to this type, and the specific capacity is relatively low.

The second type is lithium-metal alloy material. Anode materials such as Si, Ge and Sn can be used to form alloys with lithium ions. Such metals provide high specific capacity (Figure 8), but they suffer the problem of huge volume change during lithium alloying process. As a result, the mass production for commercialized LIB application is hindered due to the pulverization phenomenon.

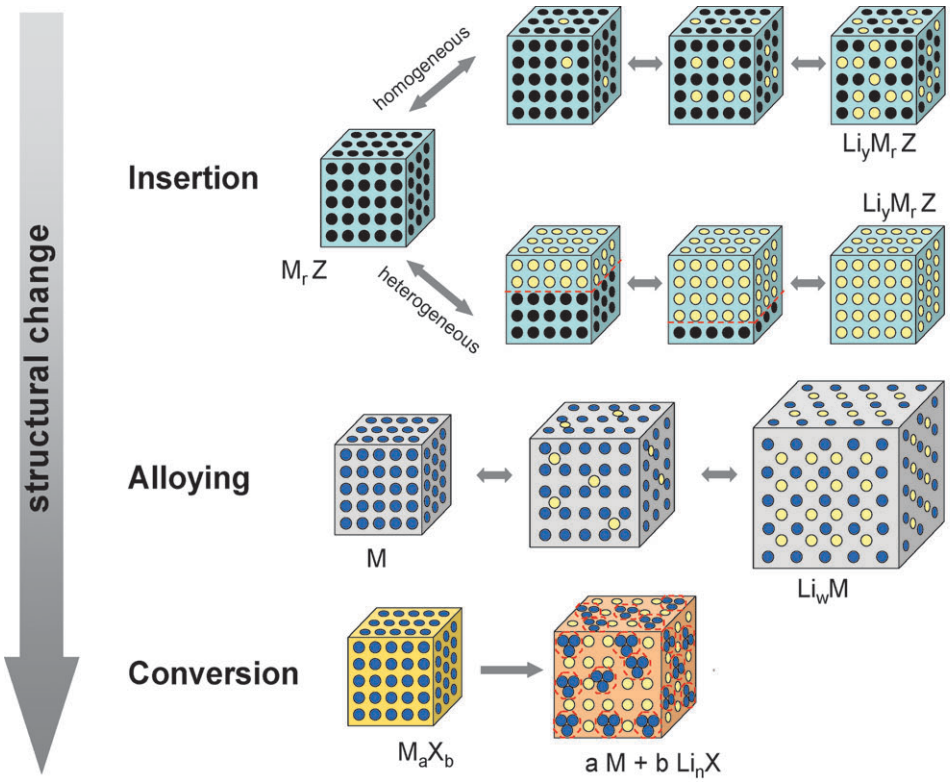

Figure 7: A schematic representation of the different reaction mechanisms observed in electrode materials for lithium batteries. Black circles: voids in the crystal structure, blue circles: metal, yellow circles: lithium.[8]

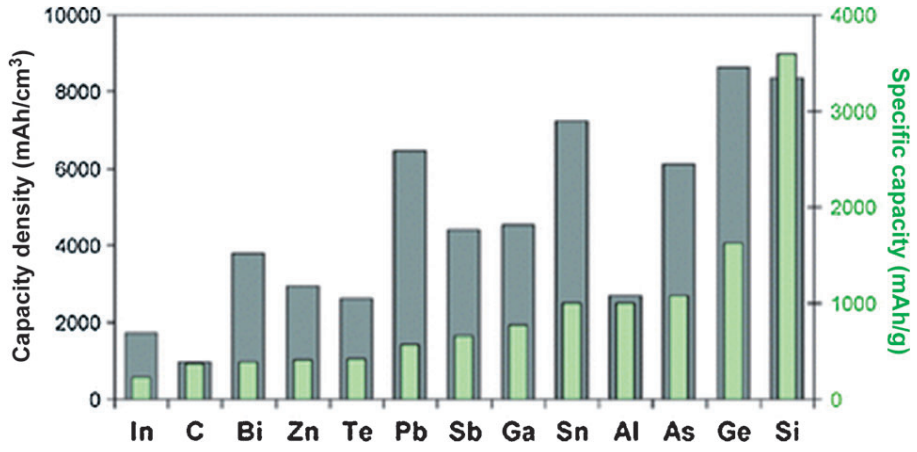

Figure 8: Specific capacities and capacity densities for selected alloying reactions. Values for graphite are given as a reference.[8]

Si is a typical alloy anode material. It has the highest known theoretical capacity (4200 mAh/g), which is almost ten times higher than graphite. But Si cycling performance is poor due to the > 300 % volume change during lithium insertion and extraction reactions.[10] Cui's group reported silicon nanowires structure as high performance LIB anodes.[10] These Si nanowires accommodate large strain without pulverization compared to Si film and particles (Figure 9). The specific capacity stabilized at 3500 mAh/g after 10 cycles. Ozin's group reported carbon inverse opals coated with amorphous silicon as macroporous composite materials. The inner carbon matrix provided a large surface area, short diffusion lengths, increased conductivity, and easy access for fast transport of reagents inside the porous structure. After long cycling, the silicon pulverization was also lowered due to this carbon backbone.[11]

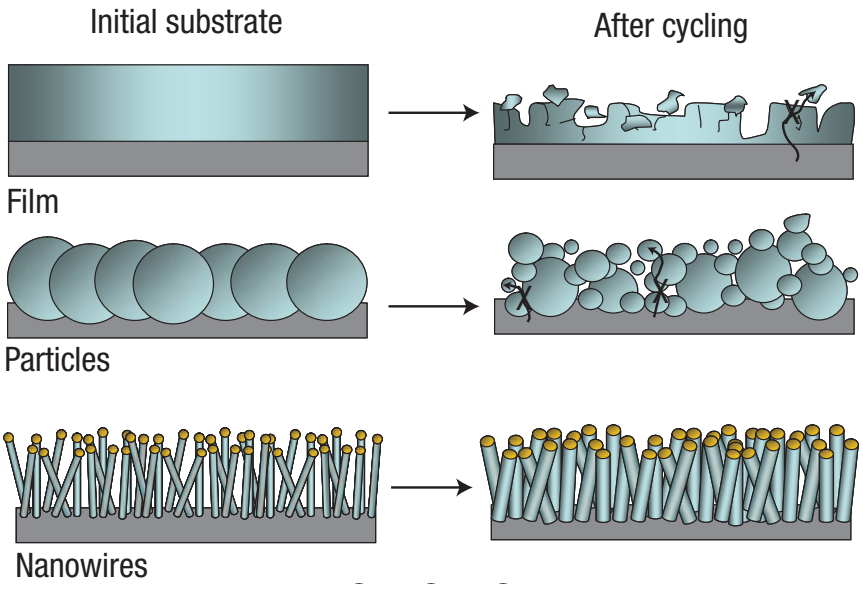

Figure 9: Schematic of morphological changes that occur in Si during electrochemical cycling.[10]

The third type is lithium-metal oxide conversion material. Metal oxides like TiO_2, Fe_2O_3 and Fe_3O_4 that undergo lithium conversion reactions deliver remarkably high specific values, due to the full reduction of transition metal oxides to metallic states. These conversion reaction based materials are promising candidates for LIB anodes in current research. Therefore, metal oxides were chosen as research topic in this thesis.

TiO_2 is also studied as LIB anode material because it has the advantages of great stability at high current density, and small volume change upon lithium insertion-desertion process. [12,13] Plus, it has the advantages of nontoxicity, affordable cost, and environmental benignity. The reaction with TiO_2 occurs at 1.4-1.8 V vs. Li/Li^+: $x\ Li^+ + TiO_2 + x\ e^- = Li_xTiO_2$. Its theoretical specific capacity is 335 mAh/g, when x=1. It's desirable to fabricate the anatase TiO_2 nanocrystal with maximum exposure of the (001) facets due to the highly anisotropic diffusion of lithium along the c-axis. The (001) facets provide the fast diffusion of lithium ions. Luo's group reported the synthesis of large ultrathin anatase TiO_2 spheres with nearly 100% exposed (001) facets (Figure 10).[14] This structure enhanced the fast reversible lithium storage. Even at a high current density of 1700 mA/g, TiO_2 spheres still delivered a specific capacity near 130 mAh/g within a voltage window of 1.0-3.0 V vs Li^+/Li.

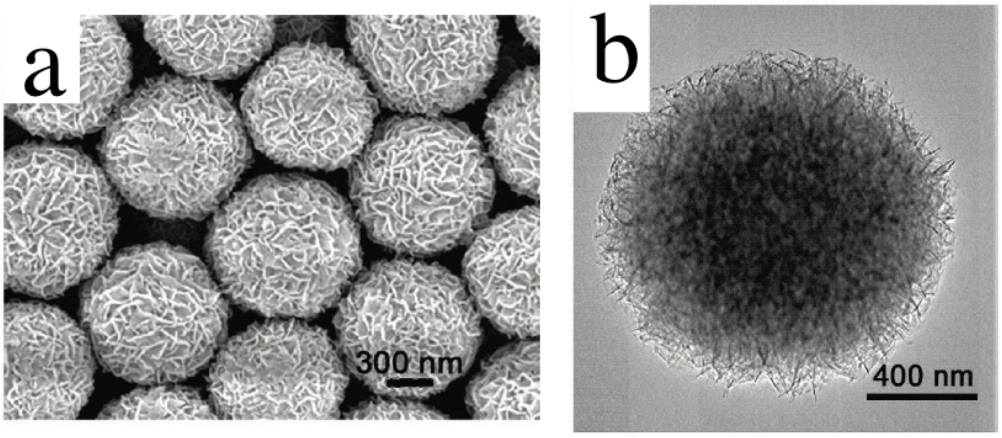

Figure 10: (a) SEM images and (b) TEM images of as-prepared anatase TiO_2 nanosheets hierarchical spheres.[14]

Table 1 summarizes various metal oxides with high specific capacities and their electrochemical reactions. SnO_2 has a theoretical specific capacity of 790 mAh/g, but it shows a large volume change of 300% during charge/discharge process, which causes electrical disconnection from current collectors. SnO_2 also lacks obvious stable discharge plateau during the reaction with lithium ions. [15,16] Co_3O_4 has similar volume change problems. In addition, large amounts of cobalt compounds (e.g. Co_3O_4,Co_2O_3 , and CoO) are potentially poisonous in the environment.

Table 1: Theoretical specific capacities and principal reactions of LIB anode materials.[12]

Materials	Theoretical specific capacities	Principal reactions
SnO_2	790 mA h g^{-1}	$SnO_2 + 4Li^+ + 4e^- \rightarrow Sn + 2Li_2O$
		$Sn + xLi^+ + xe \leftrightarrow Li_xSn$ $(0 \leq x \leq 4.4)$
Sn	994 mA h g^{-1}	$Sn + xLi^+ + xe \leftrightarrow Li_xSn$ $(0 \leq x \leq 4.4)$
Co_3O_4	890 mA h g^{-1}	$Co_3O_4 + 8Li^+ + 8e^- \rightarrow 4Li_2O + 3Co$
Fe_2O_3	1038 mA h g^{-1}	$Fe_2O_3 + 6Li^+ + 6e^- \rightarrow 3Li_2O + 2Fe$
Fe_3O_4	928 mA h g^{-1}	$Fe_3O_4 + 8Li^+ + 8e^- \rightarrow 4Li_2O + 3Fe$
Silicon	4200 mA h g^{-1}	$Si + xLi^+ + xe \leftrightarrow Li_xSi$ $(0 \leq x \leq 4.4)$

In comparison, iron oxides (e.g. Fe_3O_4 and Fe_2O_3) are environmentally friendly, abundant in nature, and they deliver high specific capacities. Figure 11 shows the iron oxide dust storm in 2009 and iron oxides precipitation in the river. In addition, different oxidation states of iron oxides (α-Fe_2O_3, γ-Fe_2O_3, Fe_3O_4, α-FeOOH, and γ-FeOOH) can be obtained via facile synthesis. Due to the variety of electronic and magnetic properties, iron oxides are widely studied in the fields of energy storage devices (anodes for LIBs), biomedicine, photoelectrochemical water splitting, and other forms of catalysis.

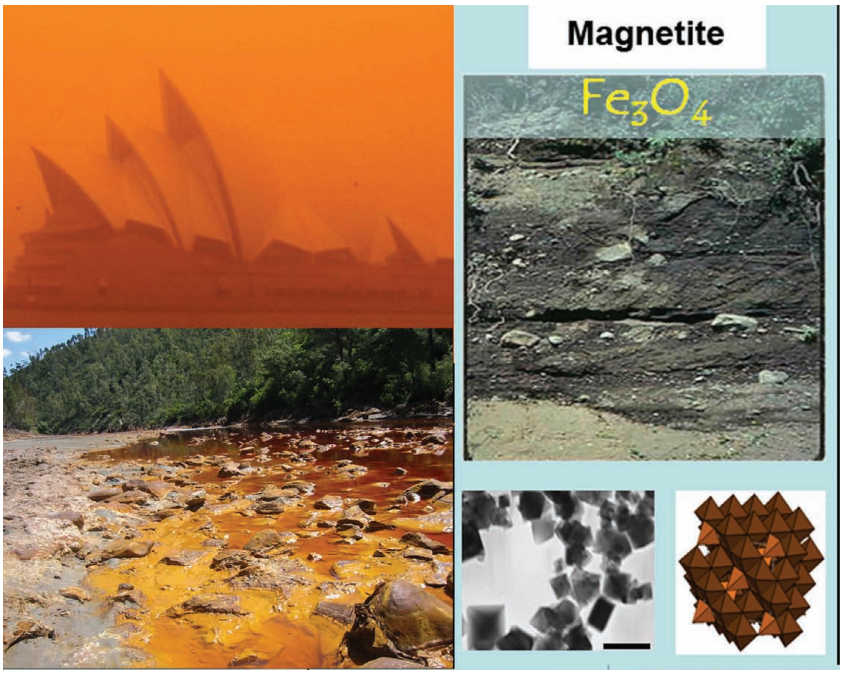

Figure 11: Upper left pictures show an iron oxide dust storm that swept over Sydney and iron oxides precipitating from the Rio Tinto water in Spain. The rest pictures shows the magnetite Fe_3O_4 and its crystal structure.[17]

Fe_3O_4 is a promising LIBs anode material, has the advantage of high theoretical specific capacity about 928 mAh/g, affordable cost, environmental friendly, abundance in nature.[17] Fe_3O_4 instead of Fe_2O_3 is chosen in this thesis because crystalized Fe_2O_3 requires annealing in air at 550 °C. But carbon material, such as graphene, will be burned when annealed in air at such high temperature. Crystalized Fe_3O_4 can be obtained via annealing in inert atmosphere like Ar, which is compatible with carbon. Since our research focuses on graphene and CNT carbon matrix, Fe_3O_4 is a better choice compared with Fe_2O_3. But Fe_3O_4 belongs to volume variation materials during lithium insertion and desertion process. The redox chemical reaction is: $Fe_3O_4 + 8e^- + 8Li \leftrightarrow$

$3Fe + 4Li_2O$. This volume change from Fe_3O_4 to Fe leads to fading specific capacity during charge/discharge process, which is a major drawback as LIB anodes. In addition, the conductivity of Fe_3O_4/Fe/Li_2O is low, and conductive carbon matrix is required as electrode material. To solve the above problems, in this thesis we use conductive carbon matrix to form carbon-iron oxide composite. Examples of current research status of carbon-iron oxides are discussed in Section 1.5.

1.2 Graphene

The Nobel Prize in Physics for 2010 was awarded to Geim and Novoselov for their research in the 2D carbon material graphene. Graphene is known as the parent of all graphitic forms such as fullerene, carbon nanotubes, and graphite (Figure 12).[18,19] Graphene can be stacked together to form 3D graphite, rolled up to form 1D nanotubes, and wrapped to form 0D fullerenes.[20] Their extraordinary electrical, mechanical, and thermal properties have attracted a lot of interests in research. The structure of graphene nanosheet is 2D layer of sp^2-hybridized carbon atoms arranged in a hexagonal lattice, which is a unique nanoscale building block (Figure 14, bottom). There are several approaches to produce individual graphene sheets (Figure 13) and functionalized derivatives, such as mechanical exfoliation[21], epitaxial growth, chemical vapor deposition (CVD)[22,23], and chemical exfoliation of graphite oxides.

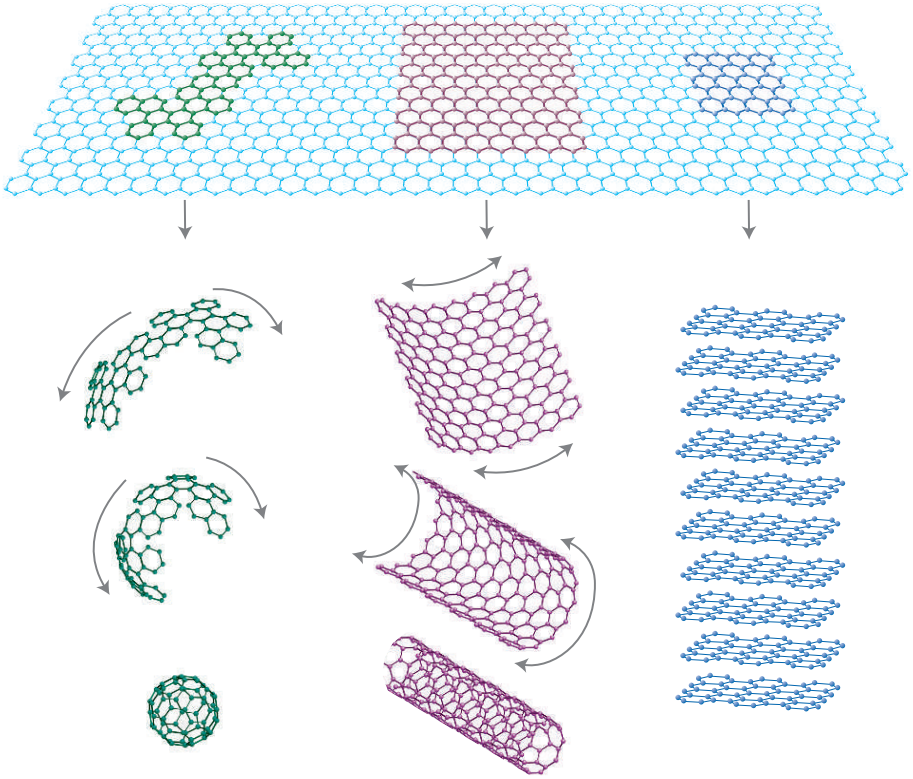

Figure 12: Graphene is a 2D building material for carbon materials of all other dimensionalities. It can be wrapped up into 0D buckyballs, rolled into 1D nanotubes or stacked into 3D graphite.[24]

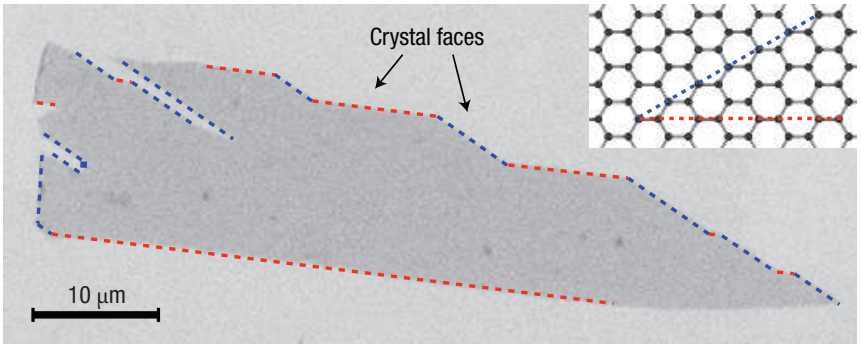

Figure 13: Scanning electron micrograph (SEM) of a relatively large graphene sheet. Most of the crystal's faces are zigzag and armchair edges as indicated by blue and red lines in the inset.[24]

Graphene oxide (GO) is usually used as a precursor for chemically derived graphene synthesis. GO contains oxygen groups including epoxy, hydroxyl, and carboxyl groups on edges and planes (Figure 14, top).[25] Figure 15 shows the process to prepare aqueous graphene dispersion from graphite. Graphite is first oxidized to form graphite oxide with larger interlayer distances, followed by exfoliation in water with sonification. The carboxylic acid and phenolic hydroxyl groups on the surface GO will be ionized, forming negatively charged GO sheets. This GO aqueous dispersion is stable and homogeneous due to electrostatic repulsion. Then GO can be easily converted to graphene via chemical reduction in hydrazine or annealing under reducing atmosphere in a tube furnace. [25,26] Upon reduction treatment, the oxygen groups are removed, and the conductivity is improved. Such graphene sheets can be assembled into freestanding paperlike films via flow-directed filtration. The film is shiny and flexible after peeling off from the filtration membrane (Figure 16).

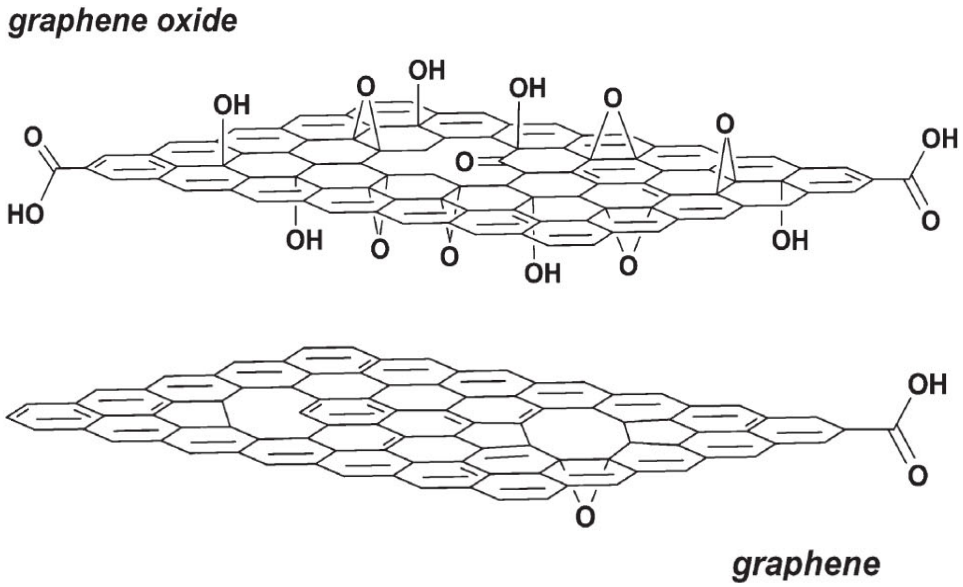

Figure 14: Schematic model of a graphene oxide sheet and graphene.[27]

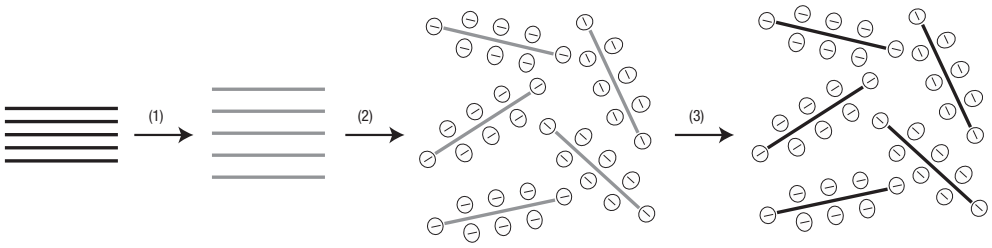

Figure 15: Scheme showing the chemical route to the synthesis of aqueous graphene dispersions. (1) Oxidation of graphite (black blocks) to graphite oxide (lighter coloured blocks) with greater interlayer distance. (2) Exfoliation of graphite oxide to obtain GO colloids that are stabilized by electrostatic repulsion. (3) Controlled conversion of GO to conducting graphene colloids through deoxygenation by hydrazine reduction.[28]

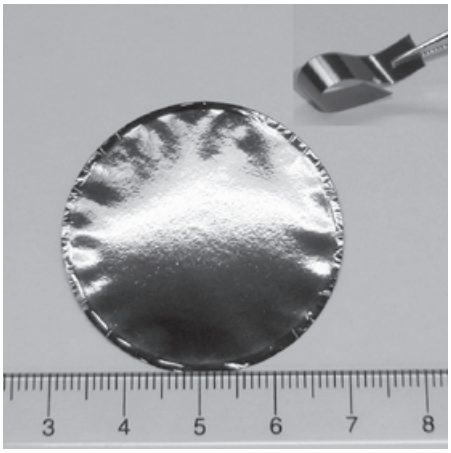

Figure 16: A 10-μm-thick chemically converted graphene film prepared by vacuum filtration. The film exhibits a shiny metallic luster. A strip (top inset) cut from the film is bent to demonstrate its flexibility.[28]

Graphene based composite materials have been widely studied in recent years.[29-33] For lithium ion battery applications, chemically derived graphene sheets generally have been hybridized nanoparticles to form composites owing to their ease of preparation and processing. Graphene sheets often serve as ideal platforms to accommodate other metal oxide guests[34], such as TiO_2[35], Fe_3O_4[36], $Ni(OH)_2$[37], Co_3O_4[38,39], MnO_2[40], SnO_2[41], and RuO_2[42]. Moreover, their two-dimensional edge plane sites assist Li-ion adsorption and diffusion.[34] Examples of metal oxide-graphene materials for LIBs will be discussed in Section 1.5.

1.3 Carbon nanotubes

CNTs can be considered of as graphene sheets seamlessly rolled into a cylindrical shape (Figure 17).[43] Generally, CNTs can be classified into single-walled carbon nanotubes (SWCNTs, $0.7 < d < 2$ nm) and multi-walled carbon nanotubes (MWCNTs, 1.4

< d < 150 nm).[44] Depending on the chirality along the graphene sheets, CNTs could be semiconducting or metallic.

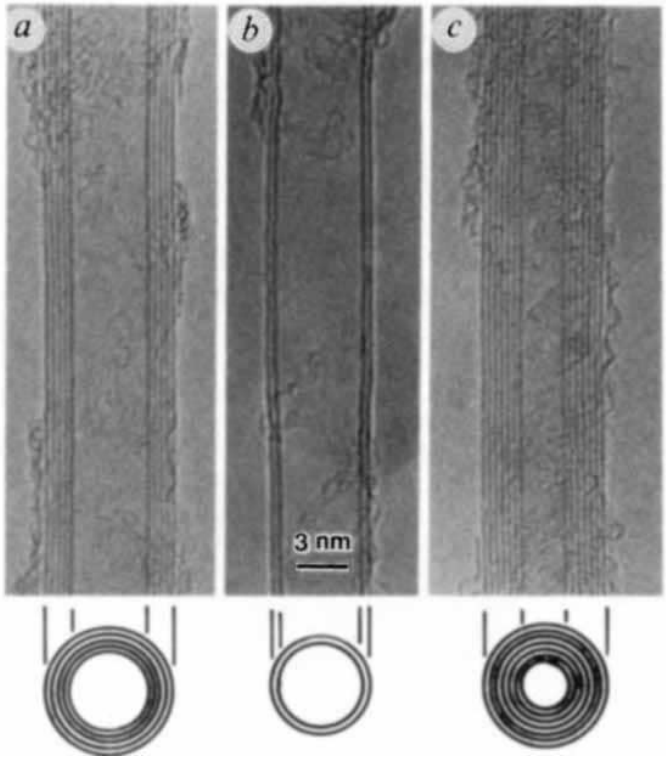

Figure 17: CNTs consisting of (a) 5 graphene sheets, (b) 2 graphene sheets, and (3) 7 graphene sheets.[43]

Currently, CNTs powders are commercially produced worldwide more than several thousand tons every year. These bulk CNTs are applied in products such as rechargeable batteries as conductive additives, automotive parts to reinforce mechanical strength, drinking water purification filters, and lightweight sporting goods. In the fields of energy storage, CNTs have versatile applications (Figure 18). For instance, MWNTs are widely used in LIBs for laptops and mobile phones. Small amounts (~1 wt. %) of

MWNT powders are mixed with $LiCoO_2$ cathodes and polymer binder in battery electrodes. Both the LIB cyclic performance and rate capability are improved because CNTs provide increased electrical connectivity and mechanical integrity[45].

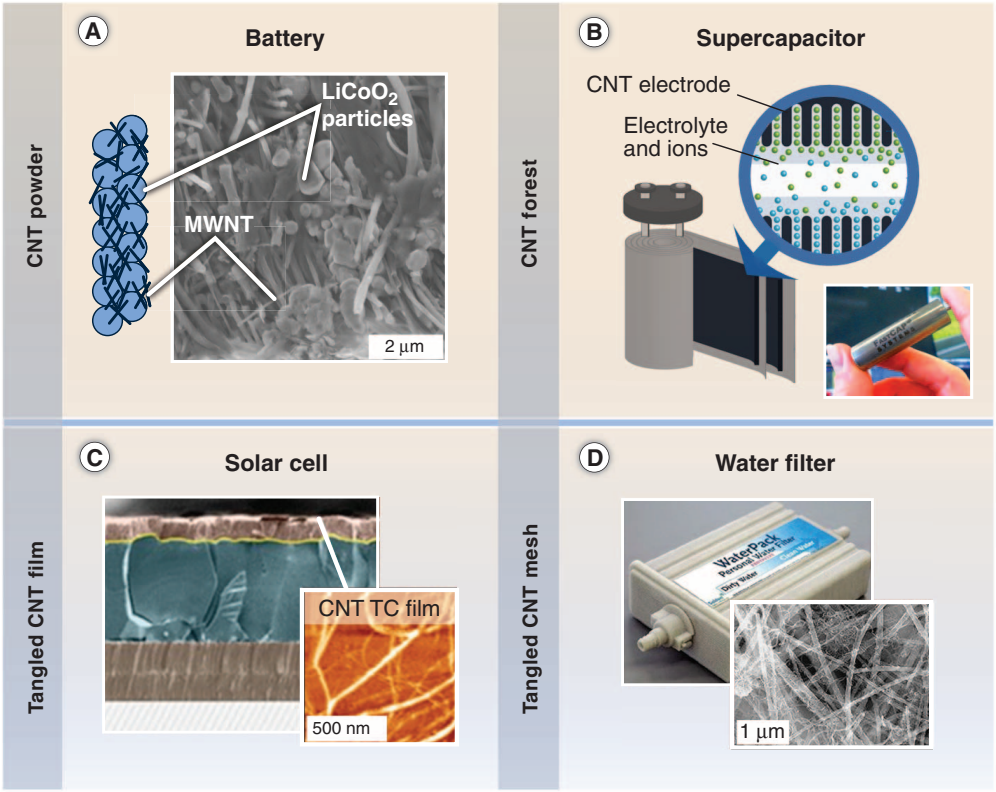

Figure 18: Energy-related applications of CNTs. (A) Mixture of MWNTs and active powder for battery electrode. (B) Concept for supercapacitors based on CNT forests. (C) Solar cell using a SWNT-based transparent conductor. (D) Prototype portable water filter using a functionalized tangled CNT mesh in the latest stage of development.[45]

Here, we will focus on the introduction of a special type of CNT family: few-walled carbon nanotubes (FWNTs). Its sidewall generally has 2 to 5 layers, and with a diameters from 3 to 8 nm, and lengths around tens of micrometers. FWNTs have excellent electronic properties and near perfect graphitization structures. [46] Even after

functionalization FWNTs still maintain the inner tubes structural integrity, and become compatible and dispersible with other materials, such as polymers and metal oxides. Our group reported the preparation of functionalized FWNT/ polyvinyl alcohol (PVA) composite film with remarkable mechanical strength. With only 0.2 wt % functionalized FWNTs, the composite film shows a remarkable reinforcement of 1650 GPa. Baek's group reported highly conductive FWNT thin film with a sheet resistance of 29400 S/m.[46] This freestanding flexible film has a tensile strength of 80 MPa and modulus of 15 GPa, respectively (Figure 19).

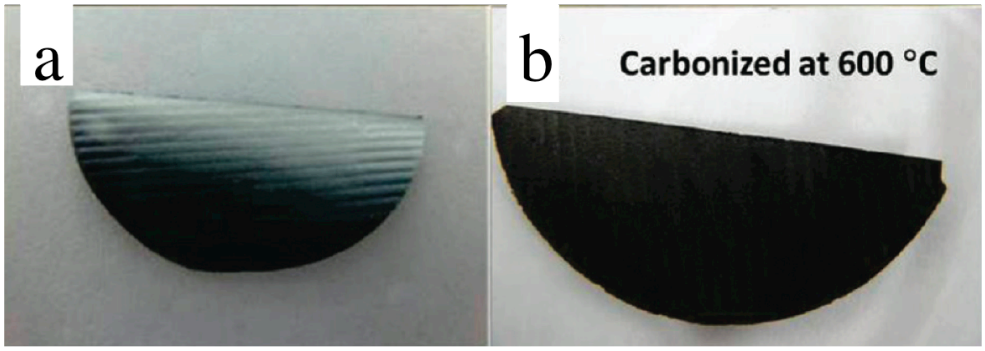

Figure 19: Digital photographs: (a) 180° folded functionalized FWNT thin film (b) functionalized FWNT thin film carbonized at 600 °C for 2 h.

1.4 Carbon aerogel

Carbon aerogel has many interesting properties, such as lightweight, continuous open porosities, high surface areas, and good conductivity. Sol-gel-derived resorcinol formaldehyde (RF) organic aerogel was first synthesized by Pekala and co-workers in 1989 (Figure 20).[47] The 3-D networks are composed of many connected colloidal nanoparticles.[48] After heat treatment, the organic aerogel converts to conductive carbon

aerogel, forming a highly open, porous, and aperiodic 3-D sponge geometry. The porosities, surface areas, and pore volumes can be tailored by controlling catalyst to solvent ratio, sol-gel polycondensation process, drying conditions, and activation process. [49,50] For instance, the catalyst to water ratio (C/W) has an effect on the aerogel pore size (Figure 21). Due to the tunable 3D hierarchical morphology and electrically conductive interconnected network, carbon aerogel is attractive host for various chemical reactions (Figure 22). It's also promising as electrode materials in LIBs, supercapacitors, advanced catalyst supports, adsorbents in wastewater treatment, and thermal insulation. Recently, the concept of carbon aerogel is further extended from RF organic aerogel to graphene aerogel, carbon nanotube aerogel and bio-mass derived aerogel, which can be found in these recent papers. [51-56] In the third chapter of this thesis, we will focus on the RF aerogel study.

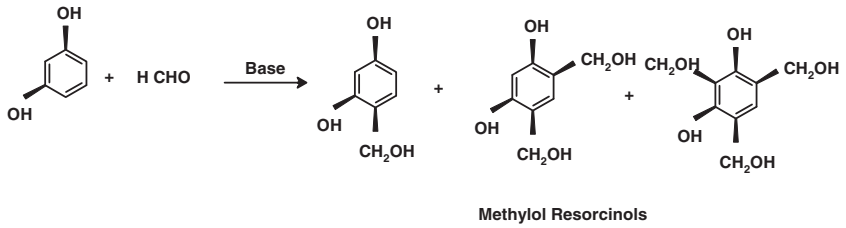

Figure 20: Reaction of resorcinol with formaldehyde under basic conditions.[57]

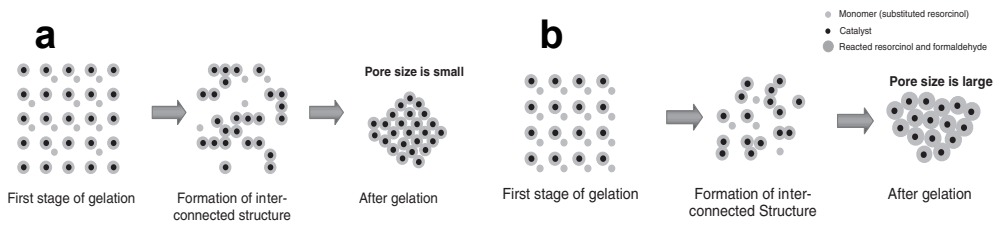

Figure 21: Model of gelation progress with (a) high and (b) low catalyst to water (C/W) ratios.[58]

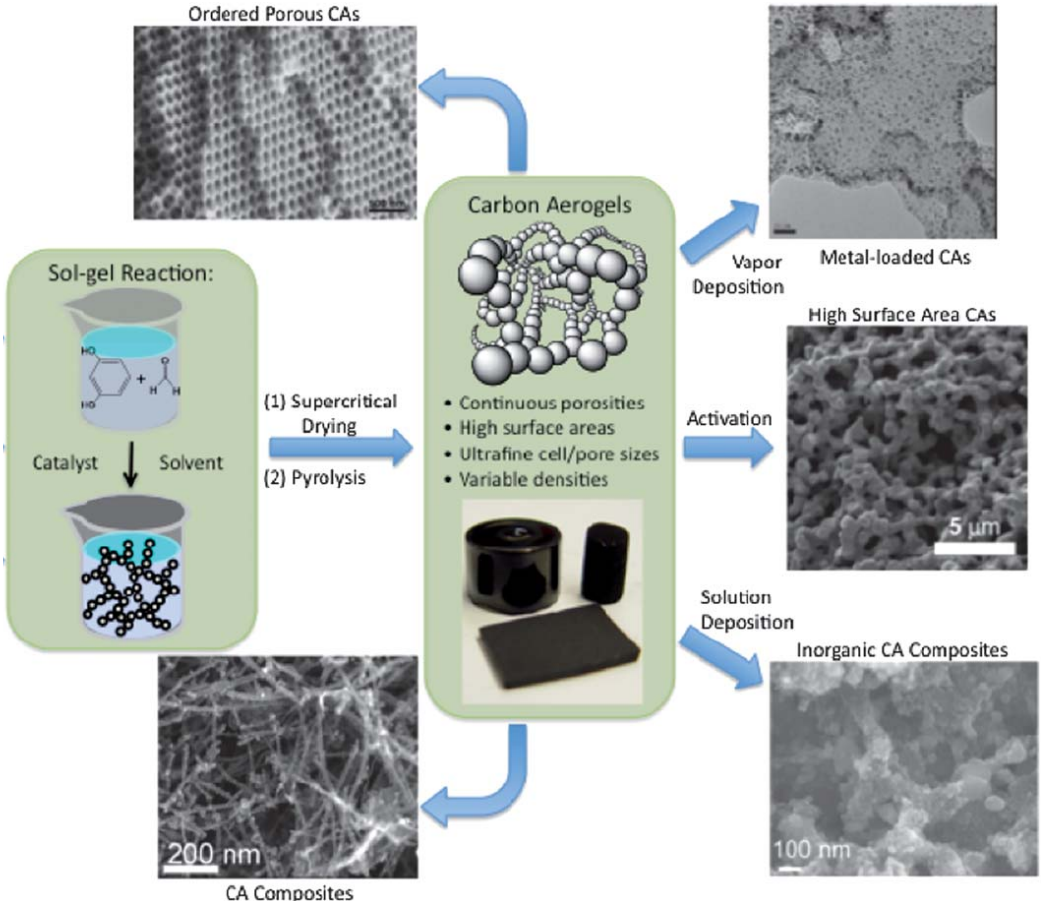

Figure 22: Synthetic scheme showing the versatility associated with carbon aerogel synthesis.[59]

Recently, Rolison's group proposed the idea to decorate the interior of porous 3D carbon aerogel materials. Carbon aerogel is an idea candidate for novel nano-architectured electrodes to enhance energy storage efficiency, because it provides a preformed carbon scaffold. They proposed a conformal electrochemical active metal oxide coating around the carbon aerogel via self-liming electroless deposition method.[60,61] Compared with carbon/metal oxide mixture and metal oxide coated carbon particles, this nano-architectured electrode design provides uninterrupted electron-conducting pathways throughout carbon scaffold (Figure 23).

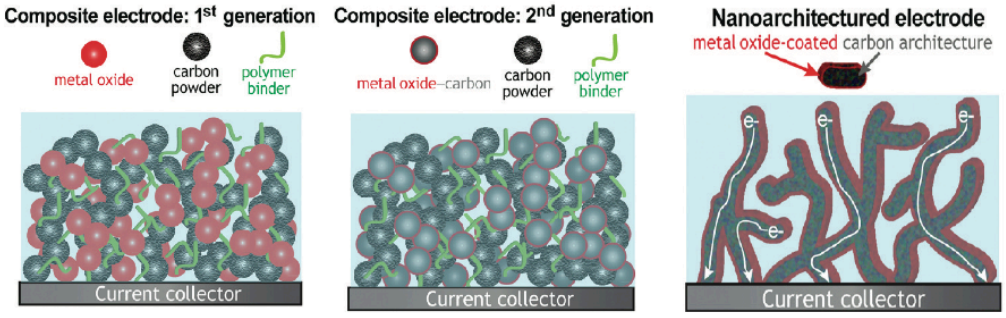

Figure 23: Electrolyte-infiltrated electrode structures incorporating electron paths, active, and inactive materials, using composites, versus a nanoarchitecture incorporating electron paths wired to the active material.[62]

1.5 Metal oxide-carbon composites

The significance of iron oxides as LIB anode materials has been discussed in the previous section. Here, the introduction mainly focuses on the iron oxide-carbon composites, and several examples of other metal oxides will be covered. Finally, the limitations of all these current composites for LIBs anodes will be summarized in this section.

To address the issues of low electronic conductivity and volume change, carbon-Fe_3O_4 composites have been studied as LIB anode materials with high specific capacities. Cheng's group reported graphene sheets wrapped Fe_3O_4, in which graphene sheets serve as flexible confinement for Fe_3O_4 volume change upon cycling (Figure 24).[36] In addition, Fe_3O_4 nanoparticles are prevented from agglomeration due to the presence of graphene sheets. This material delivered a reversible capacity of 580 mAh/g after 100 cycles at 700 mA/g. Guo's group coated mono-dispersed Fe_3O_4 nano-spindles with a uniform and continuous carbon layer around 2-10 nm, as can be seen from the scanning electron microscopy (SEM) images in Figure 25.[63] This carbon layer plays a significant role in maintaining the structure of iron oxide, and increased the electronic conductivity as well.

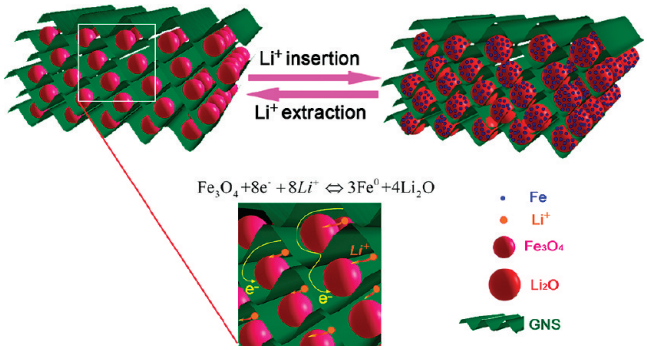

Figure 24: Schematic of a flexible structure of GNSs and Fe_3O_4 particles.[36]

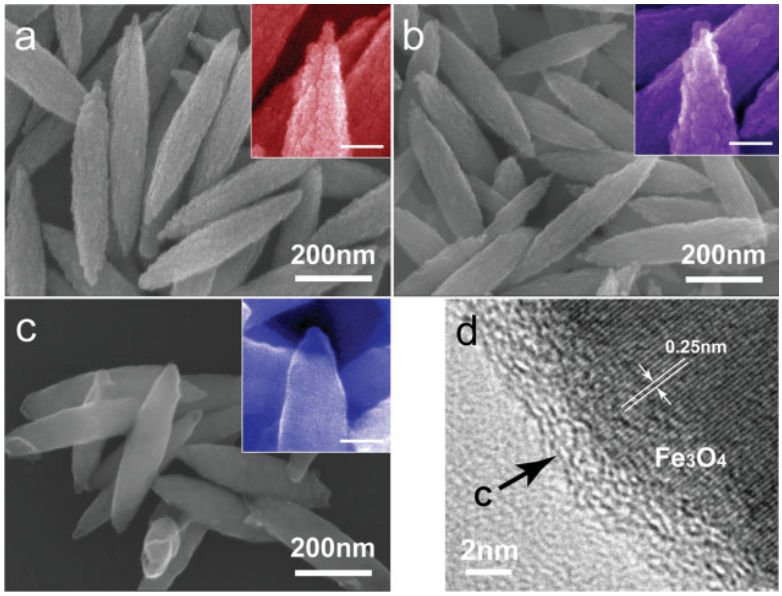

Figure 25: (a) SEM image of the as-synthesized hematite spindles. (b) SEM image of the carbon precursor coated hematite spindles. (c) SEM image of the carbon coated Fe_3O_4 spindles (Fe_3O_4–C composites). (d) High resolution TEM image of the Fe_3O_4–C composites. The insets are close views of corresponding samples, all unmarked scale bars are 50 nm.[63]

Guan's group reported a yolk–shell Fe_3O_4@C composite as high-rate LIB anode material.[64] After etching the sacrifice SiO_2 layer, there's empty space in between the Fe_3O_4 core and carbon shell (Figure 26). This interstitial void space can well accommodate the huge volume change of iron oxides during cycling process.

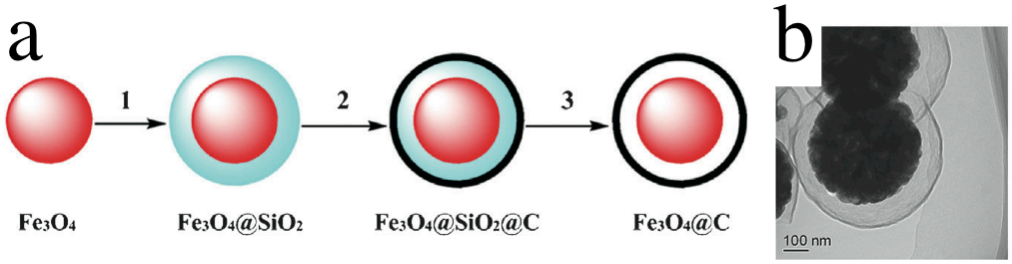

Figure 26: (a) Schematic illustration of the formation of the yolk–shell Fe_3O_4@C composite. (b) TEM images of the Fe_3O_4@C composite.[64]

Feng's group reported two-dimensional carbon-coated graphene/metal oxide hybrids for lithium storage application.[65] After the iron oxide nanoparticles grown on the graphene nanosheets, phenol-formaldehyde (PF) resol polymer coating were introduced, and finally converted to conductive carbon layer (Figure 27). This carbon layer can reserve the embedded iron oxide nanoparticles during lithium storage process, and provide conductivity between graphene sheets.

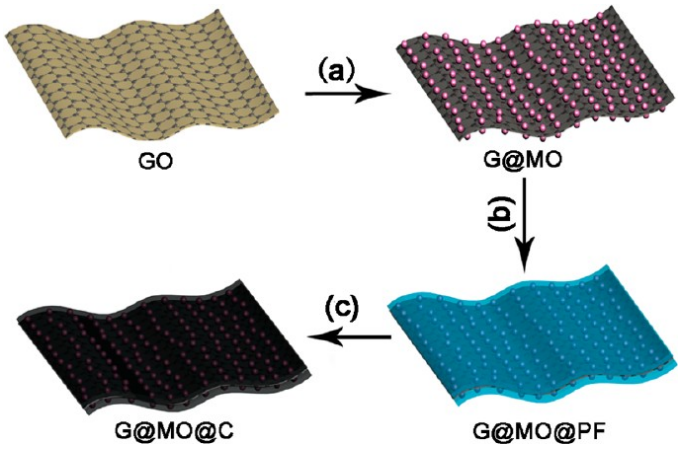

Figure 27: Schematic illustration of synthesis of 2D core-shell G@MO@C hybrids: (a) hydrolysis of metal salt on GO; (b) in-situ polymerization of PF on G@MO; (c) carbonization of PF.[65]

Similar to iron oxides, titanium dioxides also require carbon materials to provide conductivity in lithium ion battery. For example, Luo's group reported the structure of anatase TiO_2 nanosheets directly grown on the carbon nanotube backbones (Figure 28).[66] The surfaces of titanium dioxide sheets were exposed for electrochemical reaction with lithium ions, and the inner CNT provided superior electron conductivity. A reversible

capacity of around 300 mAh/g was retained at current density of 168 mA/g after 120 charge–discharge cycles in the voltage window of 0.01 to 3.00 V vs Li^+/Li.

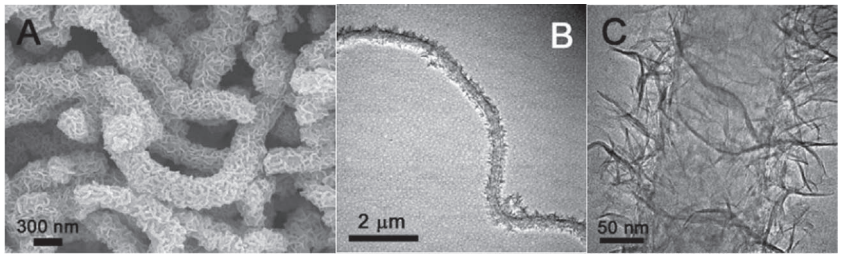

Figure 28: (a) SEM image and (b, c) TEM images of TiO_2-nanosheets[66]

Maier's group reported the structure of carbon nanotube coaxially coated by porous TiO_2 sheath (Figure [67]).[67] Moreover, CNTs not only provided conductivity for the storage material TiO_2, they efficiently stored lithium as well. The lithium storage was improved by the presence of these two intimately connected components.

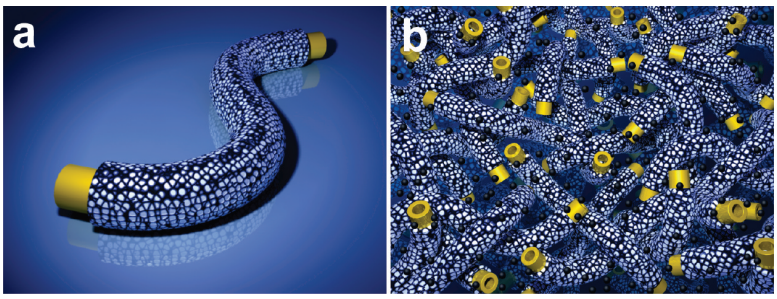

Figure [67]: (a) Schematic illustration of coaxial nanocables with electronically conducting core (CNTs) and Li+ providing nanoporous sheath (TiO_2). (b) Corresponding schematic illustration of the effectively mixed conducting 3D networks formed by the nanocables and carbon black.[67]

SnO_2 shows tremendous volume change up to 300% during the reaction with lithium ions. This drastic change hinders the application of SnO_2 as LIB anode material in real life. Several nanostructures have been proposed to solve this problem. For

instance, hollow SnO_2 nanosphere with uniform size and large void space, or a flexible coating of amorphous carbon would alleviate the pulverization issues (Figure 29).[68]

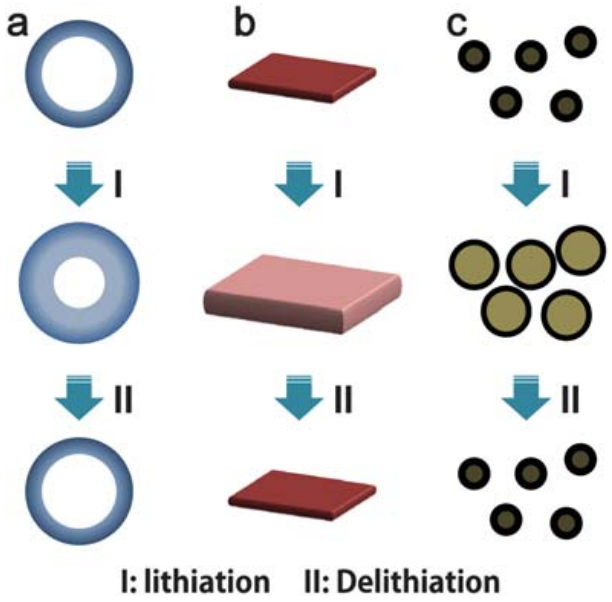

Figure 29: Schematic illustration of three basic nanostructures to alleviate the pulverization problem in SnO_2 anode materials: (a) hollow structures (b) 2D nanosheets, and (c) amorphous carbon coating.[68]

Here, it is noteworthy that all the carbon-metal oxide composites introduced here are powders. That means the slurry-cast method is necessary to test these materials as LIB anodes. The current collector, binder, and carbon additives all contribute to the total weight of the electrode in the coin cell. In the following section, lightweight CNT-metal oxide composite films will be further elaborated.

1.6 Binder-free CNT-iron oxide films

CNT has been reported to form flexible and conductive thin film itself via vacuum filtration method.[69] CNT is also studied as important component in metal oxide/carbon composite films. In fields of energy storage, CNT is well known for its excellent conductivity and mechanical strength. Due to these properties, the traditional current collector Cu foil, and conductive carbon additives (e.g. carbon black) can be removed. Thus, the binder-free CNT-metal oxide film can be directly applied as LIB anode. For instance, Lu's group reported the robust film composed of CNTs and iron oxide/carbon particles.[70] The aerosol spray method converted the iron oxide/sugar droplet precursor to Fe_3O_4/carbon microspheres, as can be seen in Figure 30. Then the microspheres were mixed with CNT and formed a robust film after vacuum filtration. This binder-free CNT/ Fe_3O_4/carbon film showed excellent stability as LIB anode even at high current density up to 6250 mA/g. However, the sizes of the microspheres were not controllable and uniform because of the aerosol spray method.

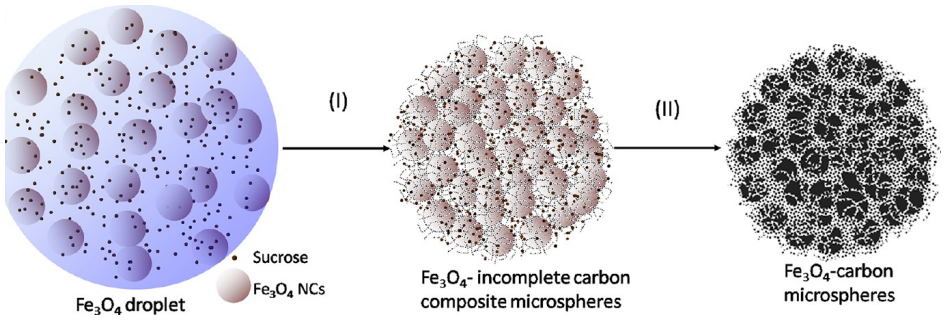

Figure 30: Scheme illustrates the formation of the Fe_3O_4/carbon microspheres.[70]

Li's group reported nanosized Fe_2O_3 decorated SWNT membrane for LIB anode.[71] SWNTs were assembled into a film on the stainless steel wire mesh before further deposition of Fe nanoparticles (Figure 31). Then the Fe-SWNTs film was annealed in air at 390 °C for 10h to oxidize the Fe nanoparticles. Finally, the Fe_2O_3 decorated SWNT membrane was peeled off from the stainless steel mesh, and directly tested as LIB anode. It delivered a specific capacity of 801 mA h/g after 90 cycles at current density 500 mA/g.

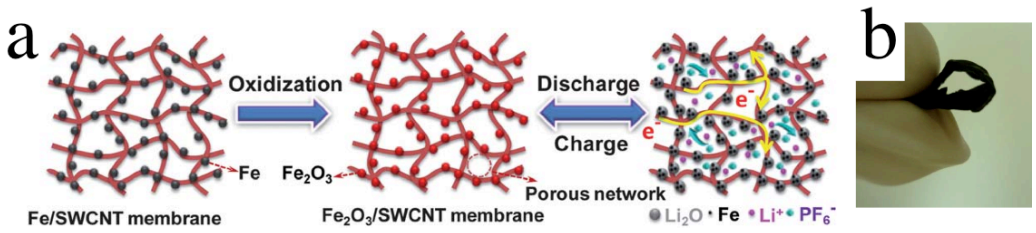

Figure 31: Schematic of the synthesis procedure and the structure of an Fe_2O_3/SWCNT membrane. Photograph showing the flexible membrane obtained after oxidation.[71]

Dillon's group reported the binder-free nanostructured Fe_3O_4/SWNT electrode for LIBs via two-step hydrothermal and vacuum filtration methods.[72] They found that annealing FeOOH nanorods mixed with 5 wt% SWNTs at 450 °C in an argon atmosphere led to the complete reduction of FeOOH to Fe_3O_4. The uniform Fe_3O_4 nanorods were uniformaly embedded in the SWNT network as can be seen in Figure 32a. Compared to microsize Fe_3O_4 particles electrode prepared in traditional slurry-cast method, the binder-free nanostructured Fe_3O_4/SWNT electrode delivered a stable

specific capacity of more than 1050 mAh/g after 50 cycles at current density 920 mA/g (1C) (Figure 32b).

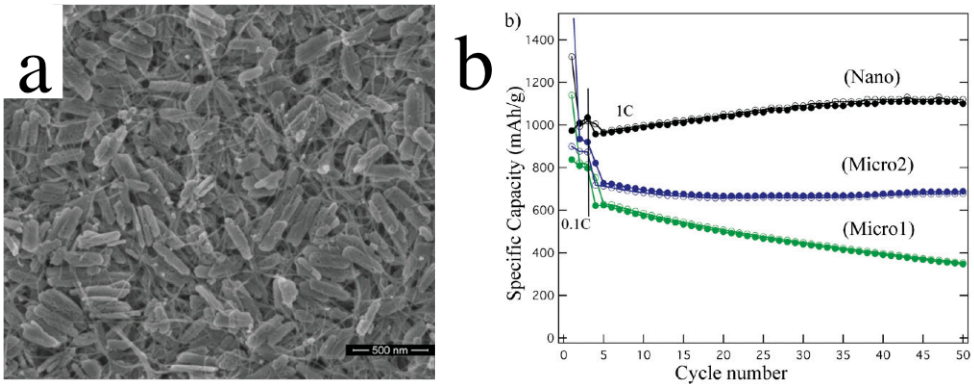

Figure 32: (a) SEM images of the nanostructured Fe_3O_4 electrode surface. (b) Comparison of specific capacity versus cycle number for various Fe_3O_4 electrodes at C rate: nano, micro1, and micro2. [72]

Wang's group reported a film prepared from CNT scaffold with conformal Fe_3O_4 sheath via magnetron sputtering method (Figure 33a).[73] After being removed from the copper cylinder this CNTs film was utilized as an excellent conducting framework, and served as current collector for the Fe_3O_4 (Figure 33b). However, the stability for both rate capability and cyclic performance needed further improvement compared with other iron oxide/carbon reported values (Figure 33c).

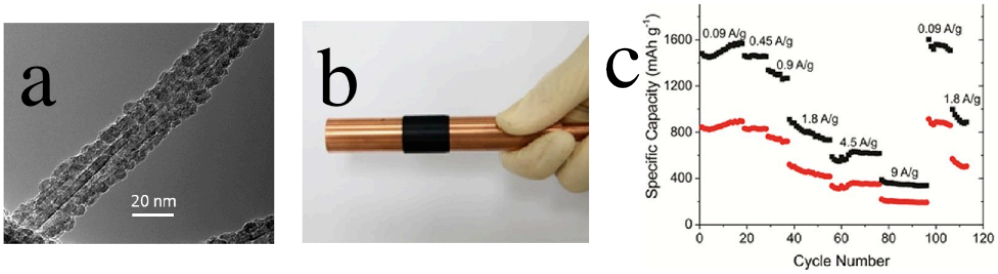

Figure 33: (a) High magnification TEM images for the precycle Fe_3O_4–CNT composite anode. (b) A photograph of the Cu cylinder wrapped with CNTs after sputtering. (c) Rate capability of Fe_3O_4–CNT. Values based on the Fe_3O_4 mass and the total anode mass are in black and red colors, respectively.[73]

Our group recently reported the robust film supercapacitor electrodes based on graphene/MnO_2/CNTs nanocomposites.[74] The surface of graphene sheets were coated with amorphous MnO_2 and then mixed with few-walled CNTs. Due to the synergistic effects from graphene, CNTs and metal oxide, this composite film was robust, highly conductive, and mechanically strong. As can be seen in Figure 34, the interconnected CNTs networks provided rapid electron conductance, while electron had to pass the insulating MnO_2 layers for the graphene/MnO_2 composite on the left.

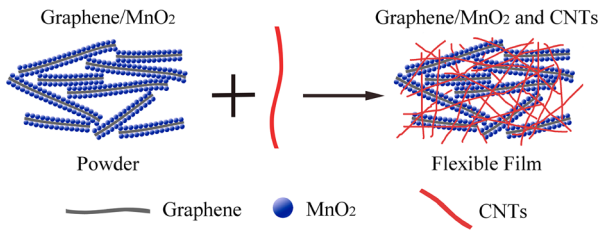

Figure 34: Schematic illustration of the fabricated flexible and conductive film using graphene/ MnO_2/CNTs.[74]

1.7 Significance of our research

In the following chapters, iron oxide/graphene/CNT film and titanium dioxide/carbon co-aerogel will be further introduced and discussed in details as lithium ion battery anodes.

The significance of the research in the second chapter is: (1) The iron oxide nanoparticles are well-crystalized, instead of amorphous. This good crystallinity greatly enhances the specific capacity of lithium ion batteries. (2) The annealing treatment plays an important role in excellent LIB performances. (3) Fe_3O_4 nanoparticles are in-situ deposited on graphene sheets in one simple step via hydrothermal reaction, and the loading densities were tunable. (4) The idea of removing current collector is further extended from supercapacitor electrodes to lithium ion battery anodes in energy storage.

The significance of the research in the third chapter is: (1) The carbon aerogel serves as a interconnected 3D conducting network. (2) The titanium oxide increases the density of the otherwise lightweight carbon aerogel and formed 3D structure as well (3) This monolith can be directly used as binder-free anode electrode in the lithium ion batteries, and the conducting carbon substitute the role of traditional current collector Cu foil. (4) This co-aerogel performance is excellent even at high current densities compared with carbon.

2. Free-standing and Highly Conductive Fe_3O_4/Graphene/CNT Film as Lithium-Ion Battery Anodes

2.1 Introduction

Lithium ion batteries (LIBs) are widely used in portable electronic devices, and are promising candidates for future hybrid electric vehicles (HEVs) and electric vehicles (EVs).[1,6] The challenges for LIBs still remain in high energy and power densities, fast charging process, stable cyclic stability, long service time.[4,75] Fe_3O_4 is intensively studied as a promising LIBs anode material because it has high theoretical specific capacity (928 mAh/g), affordable cost, environmental friendly, abundance in nature.[17] However, the application of Fe_3O_4 as LIB anode material is hindered by poor cyclic stability and low electrical conductivity.

To address these problems, it is important to design novel carbon-Fe_3O_4 composite material, as an alternative to current commercial graphite anode materials (372 mAh/g). The major benefits of nanostructures include shortened lithium ion diffusion length, increased lithium ion transport rate in the solid phase, and abundant active sites for reaction.[9,76,77] Nowadays, nanostructured carbon-Fe_3O_4 materials are extensively studied as LIBs electrodes material, such as yolk-shell Fe_3O_4@carbon,[64,78] Fe_3O_4 nanoparticles confined in mesocellular carbon,[79] and carbon coated Fe_3O_4 nanocomposites.[63,80] Carbon nanomaterials, especially graphene and carbon nanotubes (CNTs), are outstanding materials for energy storage and conversion systems.[56,81-84]

Graphene sheets have the advantages of restricting metal oxide volume change, avoiding agglomeration of Fe_3O_4 during lithium alloying process.[85] Moreover, the large surface area of graphene sheets serves as an excellent platform to accommodate metal oxides.[34] Zhou *et al.* reported graphene nanosheets as flexible platform to relieve pulverized iron oxides,[36] and Su *et al.* have synthesized 2D carbon coated graphene/Fe_3O_4 hybrids in which graphene and carbon coating buffer the deformation of Fe_3O_4 and provide high conductivity.[65] These Fe_3O_4-carbon composites are made into electrode by slurry casting method, in which conducting carbon additives (e.g. carbon black), polymeric binder, and current collector (e.g. Cu foil) are necessary. However, these components add to extra weight in the electrode and their contributions to high specific capacity is small.

Recently, CNTs are exploited as both conducting additives and current collectors in place of traditional carbon black or metal foil for next-generation flexible devices in energy storage.[45,71] The incorporation of CNTs into flexible film improves the film's overall electrical conductivity, mechanical stability and cyclic performances. Currently, several synthetic methodologies have been reported for such CNTs based flexible films. For example, magnetron sputtering synthesis of Fe_3O_4 sheath on aligned CNTs film for LIBs,[86] aerosol-sprayed Fe_3O_4-carbon particles mixed with CNT to form a robust film with excellent lithium storage performances,[70] annealing FeOOH and SWNT to form Fe_3O_4 embedded SWNT nets with stable LIB performances even at high current

density.[72] Overall, in spite of above great improvements, it is highly desirable to achieve flexible binder-free nanostructured Fe_3O_4/graphene/CNT film with excellent conductivity to deliver high specific capacity LIB anodes. Here, Fe_3O_4 instead of Fe_2O_3 is studied because crystalized Fe_2O_3 required annealing in air around 550 °C. Graphene, however, cannot survive such a high temperature when exposed to air. For crystalized Fe_3O_4, the annealing condition is around 500-600 °C in inert atmosphere such as Ar.

Previously our group reported the synergistic effect of MnO_2/graphene/CNT films as flexible supercapacitor electrodes.[74] The MnO_2 is amorphous without annealing process. Here, we presented a facile method to fabricate freestanding, highly conductive Fe_3O_4/graphene/CNT film as LIB electrodes via solvothermal reaction and vacuum filtration. The graphene-CNT networks buffer the strain from deformation of well-crystalized Fe_3O_4, keep the whole electrode material highly conductive and active, provide fast ionic and electronic pathways during alloying reaction with lithium. This binder-free film is studied as outstanding LIB anodes without metal current collector.

2.2 Experimental section

2.2.1 Preparation of graphene oxide

The Hummer's method has been reported before. Basically, 3.0 g graphite flakes (1.5 wt.%) and 1.5 g $NaNO_3$ (1.0 wt.%) were added into 75 ml H_2SO_4 with ice bath. Then 9.0 g $KMnO_4$ (3.0 wt.%) were slowly added. The mixtures were stirred at 35 °C for 1.5h. Next, 140 ml H_2O was carefully added drop wise, followed by adding another 420 ml

H_2O and 3 ml H_2O_2. Finally the graphene oxide were repeatedly washed and collected via centrifugation. The concentration of graphene oxide solution was determined to be 4.8 mg/ml.

2.2.2 Preparation of Fe_3O_4/graphene

The in-situ grown Fe_3O_4 on the graphene sheets were prepared according to previous method.[87] Briefly, 2.91 ml GO solution was centrifuged to remove the water. The rest GO was re-dispersed in 10 ml ethylene glycol and sonificated for 1h, forming a light black homogeneous solution. Next, 0.1 g $FeCl_3 \cdot 6H_2O$ was added. This solution was stirred for 2h with a magnetic bar. Then 0.72 g sodium acetate and 0.2 g polyethylene glycol were added followed by another 30 min stirring. Finally, the brownish black solution was transferred to an autoclave (20 ml in volume). The reactants were heated to 200 °C for 16h. When the autoclave was cooled down to room temperature, the black products were repeatedly washed with ethanol for at least 3 times and collected with a magnet. Then the Fe_3O_4/graphene fluids were dispersed in 25 ml ethanol.

2.2.3 Preparation of CNTs

Few-walled carbon nanotubes were prepared by a bimetallic catalysts Co/Mo supported on MgO using the chemical vapor deposition (CVD) method.[88] The details has been reported in our group's previous paper.[74] Our group member Hongbo Zhang provided the CNTs used here. The CNTs were dispersed in ethanol via tip sonification. The concentration of CNTs in ethanol was 0.13 mg/ml.

2.2.4 Preparation of Fe_3O_4/ graphene/ CNTs film

2.5 ml graphene/Fe_3O_4 solution was added to 3.0 ml CNTs solution. The mixture was sonificated 30 min before vacuum filtration. Afterward the film was carefully peeled off from the filtration membrane when completely dried. Finally the film was annealed in Ar atmosphere for 4h at 500 °C before cooling down to room temperature.

2.2.5 Preparation of commercial Fe_3O_4 electrode

The commercial Fe_3O_4 were made with a traditional slurry cast method. Fe_3O_4 purchased from Alfa Aesar were mixed with carbon black in a mortar. The polyvinylidiene fluoride (PVDF) was dissolved in the solvent N-methyl-2-pyrrolidone (NMP) as a binder. Then the paste is further mixed according to Fe_3O_4: carbon black: PVDF= 8:1:1 wt. Then mixing the slurry by repeatedly stirring the pestle. Solvent is added drop by drop during this process to avoid the evaporation of solvent. Finally, a glue-like paste is ready to be casted on Cu foil as current collector. The paste is casted onto Cu foil, dried in an oven at 73°C for 3 hours, and vacuum dried at 150 °C for 1 day.

2.2.6 Characterization

SEM and TEM images were obtained on a FEI/Phillps XL30 ESEM-FEG and TecnaiTM G2. X-ray diffraction (XRD) patterns were acquired on PANalytical X'Pert PRO MRD high- resolution diffractometer with Cu Kα radiation. BET surface area was calculated from nitrogen adsorption-desorption isotherm measurements were conducted at 77K with Micromeritics TriStar 3000. TGA spectra (TA Instruments SDT

2960) were used at a heating rate of 10.0 °C /min in air. For electrochemical measurement, the annealed Fe_3O_4/ graphene/ CNTs film was directly tested as working electrode without any carbon additives, binders, or current collector. Lithium foils served as the counter electrode and reference electrode. The electrolyte contained 1 M of $LiPF_6$ in the mixture of ethylene carbonate (EC), dimethyl carbonate (DMC) and diethyl carbonate (DEC) in 1:1:1 w/w ratio. Commercialized Celgard 2400 is used as separator. The 2032 coin cells were assembled in an Ar-filled glove box. The working electrode is usually put onto the cathode metal, followed by adding 100 μl electrolyte onto the working material. Next, carefully put the separator above the working electrode and add another 100 μl electrolytes. Then lithium metal foil is added to cover the working electrode area. Then the stainless steel disk and ring were added. Finally cover the cell with anode metal cap. Put the cell into a small plastic bag, sealed it in glove box before transferring outside. With the pressing machine, put the plastic bag together with coin cell into a mold. Use the pressure ~ 1/5 ton and hold it for 5 seconds. Thus, the coin-cell battery is ready for testing. The coin cells were cycled by a galvanostatic technique.

2.3 Results and discussion

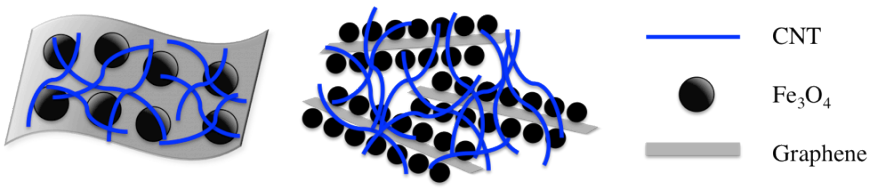

Figure 35: Structure of the Fe_3O_4/graphene/CNT film.

In spite of current progress made in Fe_3O_4-graphene and Fe_3O_4-CNT composite materials, our research focuses on conductive Fe_3O_4-graphene-CNT film in lithium ion batteries. Figure 35 illustrates the structure of Fe_3O_4/graphene/CNT film we proposed. We believe that the synergistic effects of Fe_3O_4, graphene, and CNT should help to improve the mechanical strength of the film, provide excellent electronic conductivity, and maintain high specific capacity as lithium ion battery electrodes. Last but not least, a conductive and flexible film can be used as lithium ion battery electrodes without using the conventional slurry-cast method. Instead, the film can be utilized as binder-free electrode directly, thus significantly reducing the total weight of the devices.

The major breakthroughs and differences from the previous paper published MnO_2/graphene/CNT in our group are: (1) The Fe_3O_4 nanoparticles are well crystalized, instead of amorphous MnO_2. This good crystallinity greatly enhanced the specific capacity of lithium ion batteries. (2) The annealing treatment plays an important role in the excellent LIB performances. (3) Fe_3O_4 nanoparticles are in-situ grown on graphene in one simple step via solvothermal reaction, and the loading densities are tunable. (4) The idea of binder-free electrode is further extended from MnO_2/graphene/CNT film as supercapacitor electrodes to Fe_3O_4/graphene/CNT film as lithium ion battery anodes in energy storage.

The homogeneous dispersion of Fe_3O_4-graphene composites is important for the preparation of Fe_3O_4/graphene/CNT film. In addition, the Fe_3O_4 nanoparticles need to be

closely attached to the graphene sheets so that upon cycling the performance is stable. Fe_3O_4 nanoparticles were grown on graphene sheets via a one-pot solvothermal reaction. This facile fabrication method allows in-situ growth of Fe_3O_4 on the graphene sheets. It has been introduced in the previous chapter that graphene oxide is negatively charged in the solution because there are oxygen functional groups on the surface (such as epoxyl, carbonxyl and hydroxyl groups). The positively charged Fe^{3+} ions from $FeCl_3 \bullet 6H_2O$ were attach to the graphene oxide sheet surface due to electro-static attraction. Upon the solvothermal reaction, these Fe^{3+} ions were reduced to Fe_3O_4 particles in-situ grown on the graphene sheets. The ratio of $FeCl_3 \bullet 6H_2O$ to graphene oxide precursor solution can be varied to prepare Fe_3O_4–graphene with different carbon content. The detailed study of different carbon percentage on the effect of LIB performances will be further discussed later.

Table 2: Film with different CNT content, and their specific capacities at current density of 200 mA/g.

Film	CNT content	1st cycle Discharge Specific Capacity mAh/g	2nd Cycle Discharge Specific Capacity mAh/g	5th cycle Discharge Specific Capacity mAh/g
1	7%	1320	885	795
2	10%	1243	868	841
3	18%	1170	720	473

The weight percentage of CNT in the film is a key factor in determining the properties of the film. Too little CNT will not produce a continuous film and too much

will affect the high specific capacity in LIB performances. Briefly, the Fe_3O_4/graphene composites were then mixed with CNT solution by sonification. Finally, vacuum filtration method was used to obtain a flexible Fe_3O_4/graphene/CNT film. Without adding any CNT, the Fe_3O_4/graphene composites cracked to pieces and the volume shrank to less than 50 % after vacuum filtration (Figure 36a). This problem was gradually improved by increasing CNT weight percentage. With 7% wt. CNT, the dried Fe_3O_4/graphene/CNT film 1 did not show any shrinkage. However, in the LIB study, the performance of film 1 was ordinary. For Fe_3O_4 /graphene/CNT film with 7% wt. CNT, the discharge specific capacity for 1st, 2nd, and 5th cycle is 1320, 885, 795 mAh/g respectively (Table 2). The reason for fast-fading 45% capacity loss in the first 3 cycles could be a lack of conductive electronic pathway provided by CNTs. The Fe_3O_4 is therefore not fully accessible for electrochemical reactions. Then the CNT percentage was further increased to 10% wt. The discharge specific capacity for 1st, 2nd, and 5th cycle is 1243, 868, 841 mAh/g respectively for film 2. This performance with 10% wt. CNT was more stable compared with the previous 7% wt. CNT. Finally, the CNT weight percentage was increased to 18% wt. For Fe_3O_4 /graphene/CNT film 3 with 18% wt. CNT, the discharge specific capacity for 1st, 2nd, and 5th cycle is 1170, 720, 473 mAh/g respectively. The decreasing specific capacity can be attributed to the large amount of carbon, which has much lower specific capacity than that of Fe_3O_4. Here, the optimized CNT weight percentage is around 10% wt. With 10% wt. CNT, the specific capacity was

most stable compared to that of 7% wt. and 18% wt. CNT. The cyclic and rate performance of 10% wt. CNT based film will be further studied in the following paragraphs.

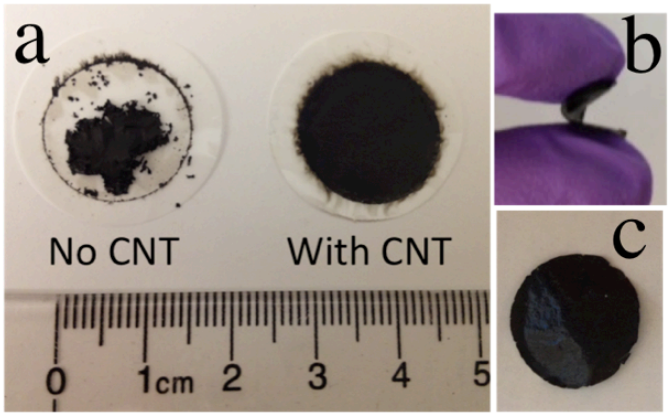

Figure 36: (a) The Fe_3O_4/graphene film cracks without CNT after filtration. (b and c) The flexible Fe_3O_4/graphene/CNT film peeled off from filtration membrane.

The total carbon amount is also important for LIB performances. Too little carbon, the electronic conductivity is not enough for the film as binder-free electrode. Too much carbon, the specific capacities of LIB fade fast because the active material iron oxide amount is not enough. To further understand the role of total carbon amount, films with different carbon weight percentage from different Fe_3O_4-graphene precursor were investigated (Table 3). Since the optimized CNT weight percentage was studied and summarized as 10% wt., the Fe_3O_4–graphene materials with different carbon weight percentage were also studied. Here we'd like to point out that the optimized CNT weight percentage was calculated to be around 10 % wt. without annealing. After the

annealing process at 600 °C in Ar atmosphere for 4 hours, there was weight loss for the film. Such weight may come from the decomposition of small functional groups from carbonaceous materials. This explains the reason for total carbon weight percentage around 10 % wt. for annealed film A. The cyclic performance of film A is plotted in Figure 37 as black square. The specific capacity continuously decreases during the first 10 cycles. For the annealed film A with 10% wt. total carbon, the 1st and 2nd discharge specific capacity was high (1239 and 843 mAh/g), but the capacity retention was poor. The 10th specific capacity suddenly dropped to 481 mAh/g. The limited amount of conductive carbon matrices cannot afford the huge volume change of iron oxides occurred during the cycling. Thus, the exposed iron oxides nanocrystals pulverized and capacity dropped. For the annealed film B with total carbon weight percentage of 30% wt., the 1st, 2nd, 5th and 10th specific capacity was 1243, 868, 841, and 823 mAh/g respectively. The capacity retention was much better compared with film A, as illustrated in Figure 37 with red circle. We think the 30% wt. carbon amount is appropriate to provide enough electronic conductivity, while assisting Fe_3O_4 to deliver a reversible high specific capacity. The detailed study of film B will be further discussed in the following paragraph. For the annealed film C with 57% wt. carbon, the specific capacity declined from 1100 mAh/g in the 1st cycle to only 342 mAh/g in the 10th cycle. This decreasing trend is due to increased graphene ratio. When carbon weight percentage is dominant (57% wt.), the iron oxides probably are fully trapped by carbon

material and become inaccessible for electrochemical reaction with lithium ions. That also explains the reason that film C specific capacity fades fast (Figure 37, green triangle). The trend is similar to that of graphite electrode performances, which generally gives lower specific capacity than iron oxide. So far, film B has the best carbon weight percentage around 30% wt. and a 10% wt. CNT. It shows excellent cyclic performance as LIB anode, which is similar with other reported optimized carbon weight percentage values.[70,80] Therefore, the composition of film B was chosen as the optimized formula for further study in my research.

Table 3: Film with different carbon weight percentage, and their specific capacities at current density of 200 mA/g.

Film	TGA carbon content	1st cycle Discharge Specific Capacity mAh/g	2nd Cycle Discharge Specific Capacity mAh/g	5th cycle Discharge Specific Capacity mAh/g	10th cycle Discharge Specific Capacity mAh/g
A	10%	1239	843	614	481
B	30%	1243	868	841	823
C	57%	1100	622	427	342

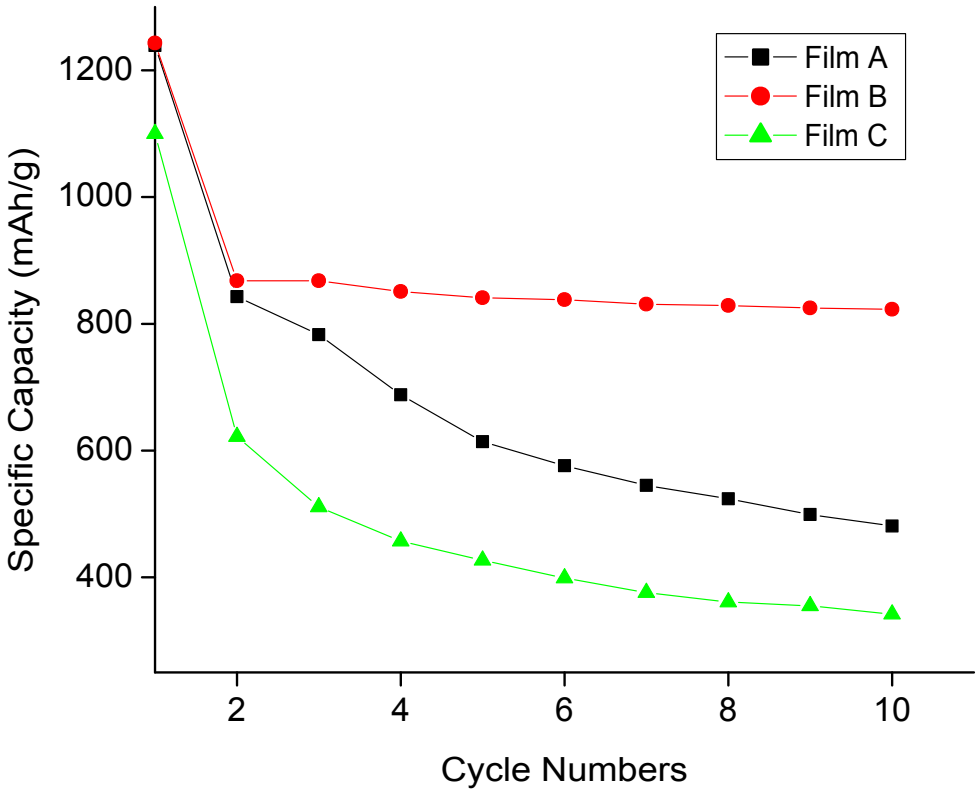

Figure 37: Cyclic performance of Fe_3O_4/graphene/CNT film with different carbon weight percentage at current density of 200 mA/g. Film A, B and C has total carbon content of 10, 30, and 57 % wt. respectively.

The annealing effect on the crystallinity is also found to be a critical factor in the LIB study. Without annealing, the conductivity of the film is too low as binder-free anode material. With high temperature annealing, the electronic conductivity improves. The annealing temperature also affects the LIB performances. Poor iron oxide crystal structure leads to poor LIB performance, and excellent crystal structure gives improved and reversible capacity. The as-made Fe_3O_4/graphene/CNT film without heat treatment showed a high sheet resistance (800 Ω/□) and poor crystallinity. With such a high sheet

resistance, it was very difficult to apply the film as binder-free electrode because the electronic conductivity was poor. Since the annealing temperature range for crystalized Fe_3O_4 is from 500-600 °C in inert atmosphere depending on different Fe_3O_4-carbon materials. The film was annealed in tube furnace in Ar atmosphere at 500 °C for 4 hours. The corresponding XRD pattern of the Fe_3O_4/graphene/CNT film can be seen in Figure 38a. The peaks matches well with that of standard magnetite phase Fe_3O_4. But the peaks are not intensive, which means the crystallinity of Fe_3O_4 is weak. Actually, weak crystallinity is not good for LIB electrode. The reason is that lithium ions first insert into the crystal structure of iron oxides, and then the electrochemical reactions can prodeed. That's to say, if the crystallinity is poor, the lithium ions inserted into the iron oxide structure are limited, and the LIB performance will be affected as well. Finally, the annealing temperature is further raised to 600 °C to improve the crystallinity. Figure 38b shows the XRD pattern of the Fe_3O_4/graphene/CNT film. All the peaks are in good agreement with standard magnetite phase of Fe_3O_4. These sharp peaks confirm good crystallinity similar to commercialized Fe_3O_4. A sheet resistance of 23 Ω/□ was measured for Fe_3O_4/graphene/CNT film with a four-point probe. The graphene-CNT carbon matrix forms an efficient electron pathway to provide excellent electrical contacts for the Fe_3O_4 crystals. We believe the high-temperature heating process enhanced the connectivity between conductive carbon matrix and electrochemically active Fe_3O_4. Therefore, Fe_3O_4 crystalinity, good contact between Fe_3O_4 and conductive CNTs facilitate the excellent

performances as LIB electrodes. This annealed film thickness was measured to be 21 μm, which is a little bit thinner compared to reported values of 35 μm for CNT/iron oxide composite film.[70] The annealing process and good crystallinity are important for the film as LIB electrodes. The mechanical strength data can be seen in Figure 39. From the stress-strain curve, the stress is 520 kPa, the strain is 0.42% and the Young's modulus is calculated to be 124 MPa, which is similar to the rubber material (10-100 MPa).

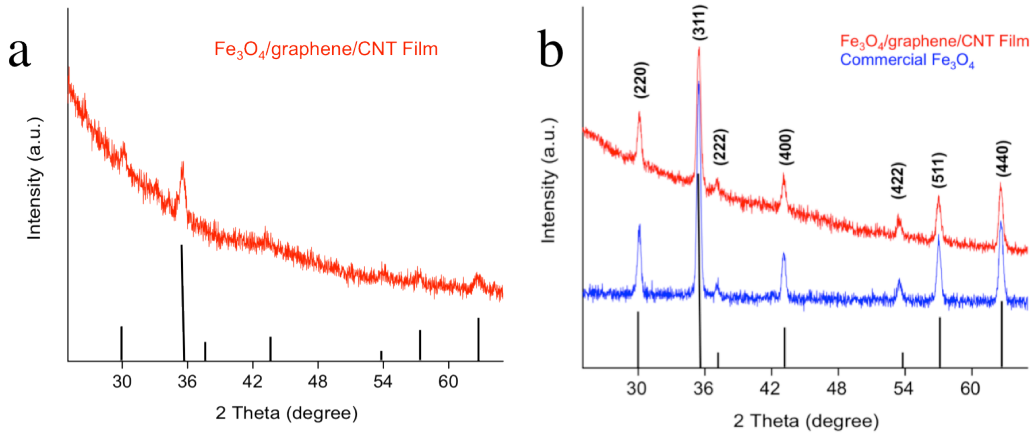

Figure 38: XRD patterns of Fe_3O_4/graphene/CNTs film annealed at (a) 500 °C and (b) 600 °C in Ar atmosphere for 4 hours.

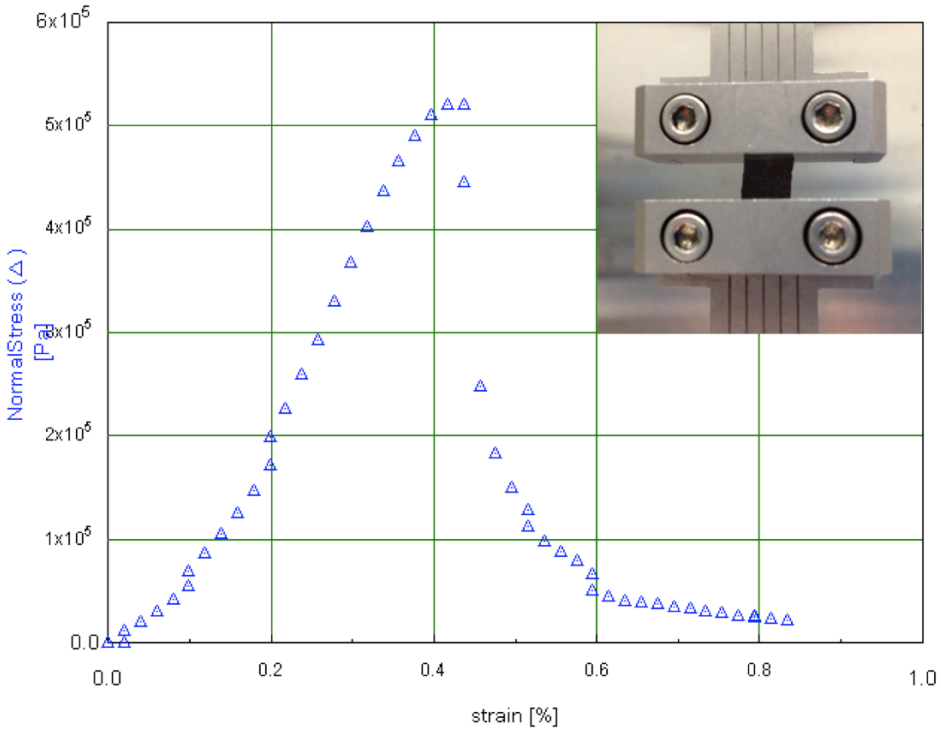

Figure 39: Stress-strain curve of the flexible Fe_3O_4/graphene/CNTs film after annealing treatment at 600 °C.

Each component in the film was characterized with microscopy techniques to provide a deeper understanding of the film structure. Figure 40a shows the transmission electron microscopy (TEM) image of functionalized few-walled carbon nanotubes with 3–5 walls prepared in our lab. These CNTs have better electric conductivity and mechanical strength compared with other types of nanotubes.[89] These CNTs have been purified to remove catalyst, and functionalized to improve dispensability in the ethanol solution. The CNTs are very clean without any catalyst residues as can be seen from TEM. In addition, the tubes are smooth and without obvious defects or damages. This can be attributed the advantages that few-walled carbon nanotubes that they keep

structural integrity of inner tubes after functionalization. Therefore, the excellent electronic conductivity and mechanical strength can be preserved and utilized. Figure 40b demonstrates the Fe_3O_4 nanocrystals homogeneously grown on graphene sheets via in-situ growth. The graphene sheet is a good platform to accommodate Fe_3O_4 nanocrystals without aggregation, forming a nice Fe_3O_4-graphene dispersion. The one-pot solvothermal fabrication method is facile and also allows controlled density of both graphene and iron oxides. The annealed Fe_3O_4/graphene/CNT film is re-dispersed via sonification, as can be seen in Figure 40c. The CNTs entangled with Fe_3O_4/graphene sheets. The iron oxides were still homogeneously dispersed on the graphene sheets even after sonification and re-dispersion. The reason is that the iron oxides closely anchored on the graphene sheets during the solvothermal reaction. In addition, the CNTs also connected and entangled well with iron oxide and graphene, to provide electronic conductivity and mechanical strength as a composite film. Figure 40d is SEM image of Fe_3O_4/graphene/CNT film. From the fractured gap in the film, interconnected CNTs can be clearly observed. This picture reflects that CNTs form a strong and robust network to well connect the Fe_3O_4-graphene material. The film surface is smooth and full of Fe_3O_4 crystals. The sizes of Fe_3O_4 crystals are homogeneous and without obvious micro-scale aggregation. The SEM image also matches well with the TEM images that the film has interconnected graphene-CNT network with homogeneously dispersed Fe_3O_4 nanoparticles. In addition, thermal gravimetric analysis (TGA) shows that the annealed

Fe_3O_4/graphene/CNT film contains about 30 wt.% carbons. Brunauer-Emmett-Teller (BET) specific surface area of the film is 130 m^2/g by nitrogen isothermal adsorption, which is much higher than commercial Fe_3O_4 (17 m^2/g).

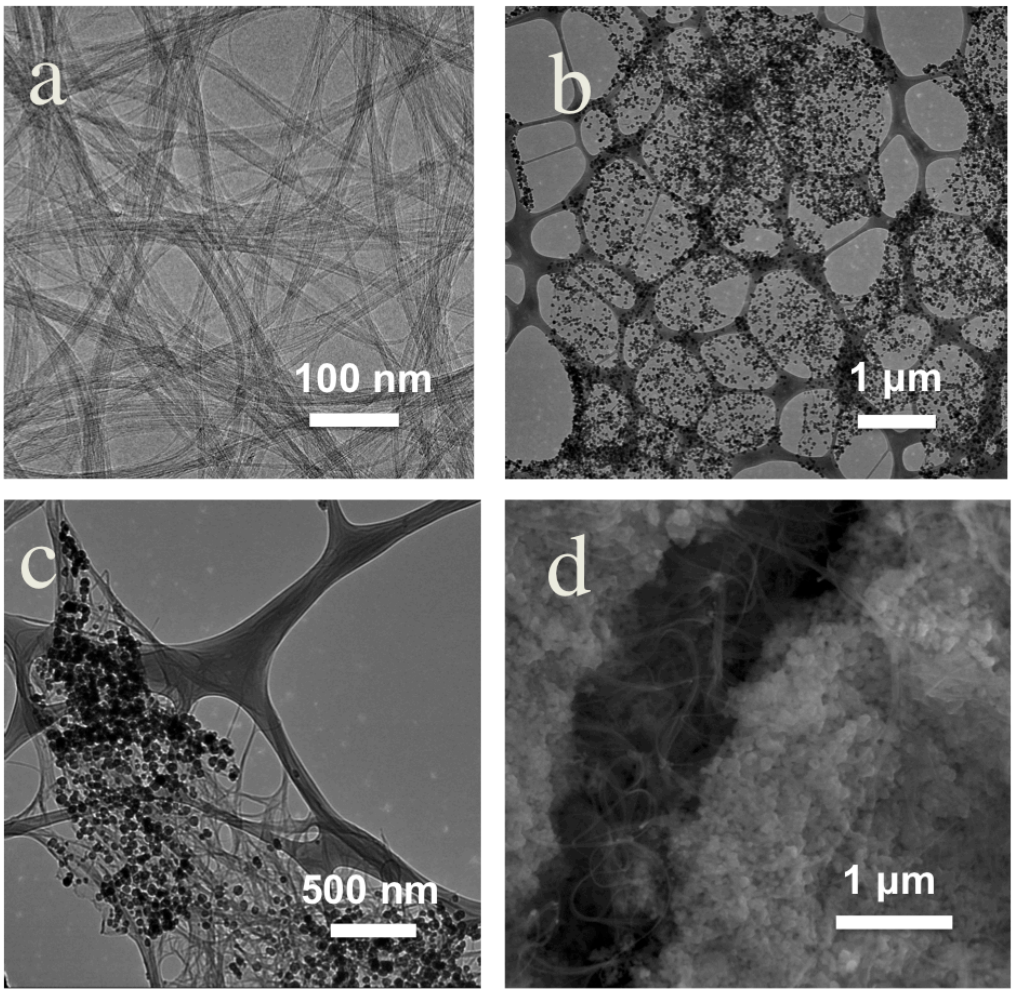

Figure 40: TEM images of (a) carbon nanotubes, (b) Fe_3O_4 nanoparticles grown on graphene sheets, (c) annealed Fe_3O_4/graphene/CNTs film re-dispersed via sonification, (d) SEM image of a fractured annealed Fe_3O_4/graphene/CNTs film highlighting the interconnected CNTs network.

The electrochemical performance study of Fe_3O_4/graphene/CNT film is carried out to further understand the advantages of binder-free film as LIB anode. Figure 41 shows the assembling of binder-free coin cell for lithium-ion battery study. Basically, the Fe_3O_4/graphene/CNT film is directly used as working electrode without conventional slurry-cast method for electrode preparation. The extra weight is eliminated including Cu foil as current collector, polymeric binder and carbon black as conductive additives. In between the Li foil and film, there is an electrolyte-soaked separator. It's intended to avoid direct contact between working electrode and counter/reference electrode. The electrolyte is 1 M of $LiPF_6$ in EC/DMC/DEC (1:1:1 w/w ratio). The coin cell battery is assembled in Ar-filled glove box.

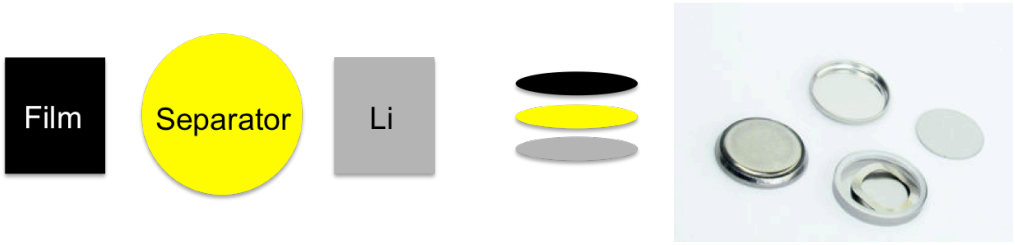

Figure 41: Illustration for binder-free coin cell structure.

The electrochemical properties were studied by galvanostatic charge-discharge cycling in a coin cell with Li foil as counter electrode between 0.01 and 3.00 V vs Li^+/Li. The specific capacity calculation is based on the weight of the total weight of the film. This film has contains about 30 wt.% total carbon after annealing treatment.

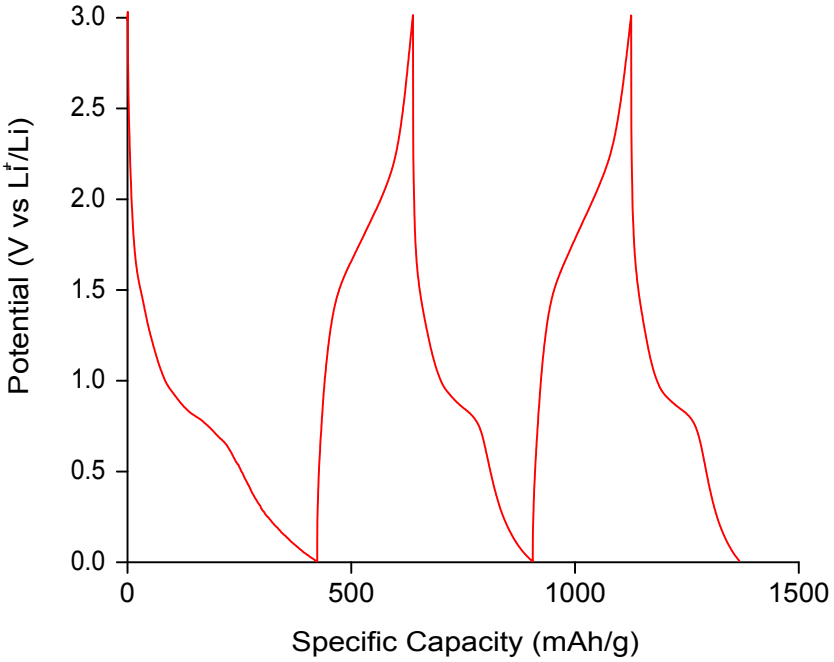

Figure 42: The charge and discharge curves of the Fe_3O_4/graphene/CNT film annealed at 500 °C for 1st, 2nd, and 3rd cycle at 200 mA/g.

Figure 42 shows the charge-discharge curve of Fe_3O_4/graphene/CNTs film annealed at 500 °C film. There's no obvious plateau at 0.8 V vs Li^+/Li, which belongs to the electrochemical reaction between lithium ion and Fe_3O_4. As a result, the discharge specific capacity for the first cycle is less than 500 mAh/g, which is much less than the theoretical specific capacity of Fe_3O_4 (928 mAh/g). In the potential window of 1.5 – 1.0 V vs Li^+/Li, the lithium ions inserted into the crystalized structure first, according to $xLi^+ + Fe_3O_4 \rightarrow Li_xFe_3O_4$. For the film annealed at 500 °C, the crystallinity is poor. So there is limited lithium ions inserted into the Fe_3O_4 crystals for further electrochemical reactions. Considering the weak crystallinity in the XRD pattern, the major reason for this low specific capacity is the lack of crystallinity.

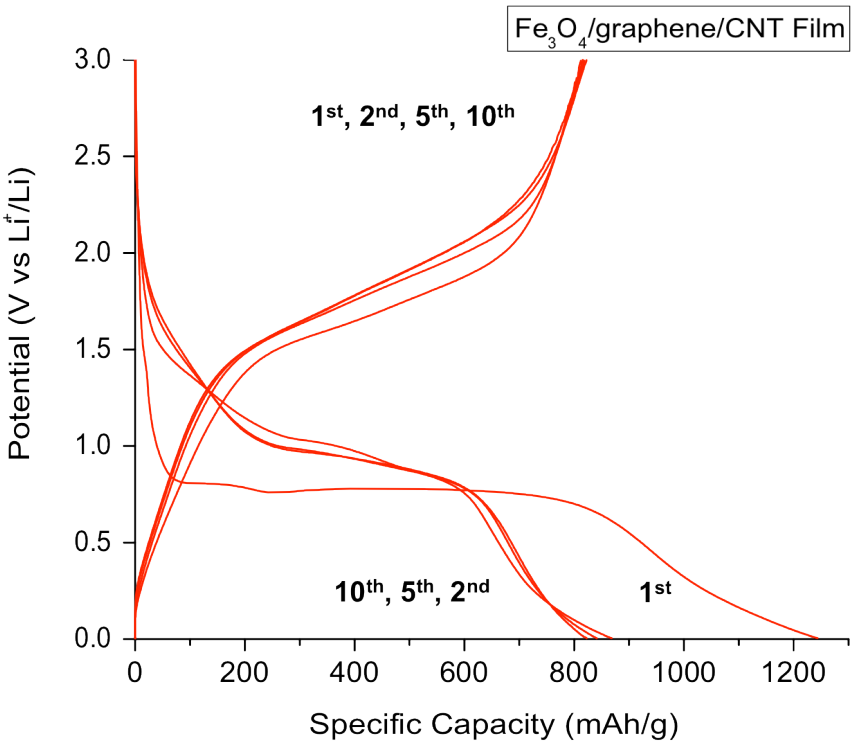

Figure 43: The charge and discharge curves of the Fe_3O_4/graphene/CNT film annealed at 600 °C for 1st, 2nd, 5th and 10th cycle at 200 mA/g.

In comparison, Figure 43 shows the charge and discharge curves of Fe_3O_4 /graphene/CNT film annealed at 600 °C with excellent crystallinity. The plateau at 0.8 V vs Li^+ /Li is much longer and smoother than that of film annealed at 500 °C. At a current density of 200 mA/g between 0.01 and 3.00 V vs Li^+ /Li, the first charge and discharge specific capacity were 1243, and 868 mAh/g. The irreversible capacity loss is 30%, as generally observed for iron oxides.[90] Fe_3O_4 can uptake 8 Li^+ to deliver a theoretical specific capacity of 928 mAh/g, and the film's first charge value corresponds to 10.8 Li^+. The first specific capacity value is higher than theoretical because of the electrolyte decomposition and irreversible Li^+ loss during the surface electrolyte interface (SEI)

formation.[72] The redox chemical reaction is: $Fe_3O_4 + 8e^- + 8Li \leftrightarrow 3Fe + 4Li_2O$. The long plateau at 0.8 V in the first discharge curve can be attributed the reduction of Fe^{3+} and Fe^{2+} to Fe^0.[64] Then the specific capacity stabilized around 823 mAh/g for the 10th cycle. In the window of 1.2-2.2 V vs Li^+ /Li, the reverse charge process proceeded according to reversed electrochemical reaction.

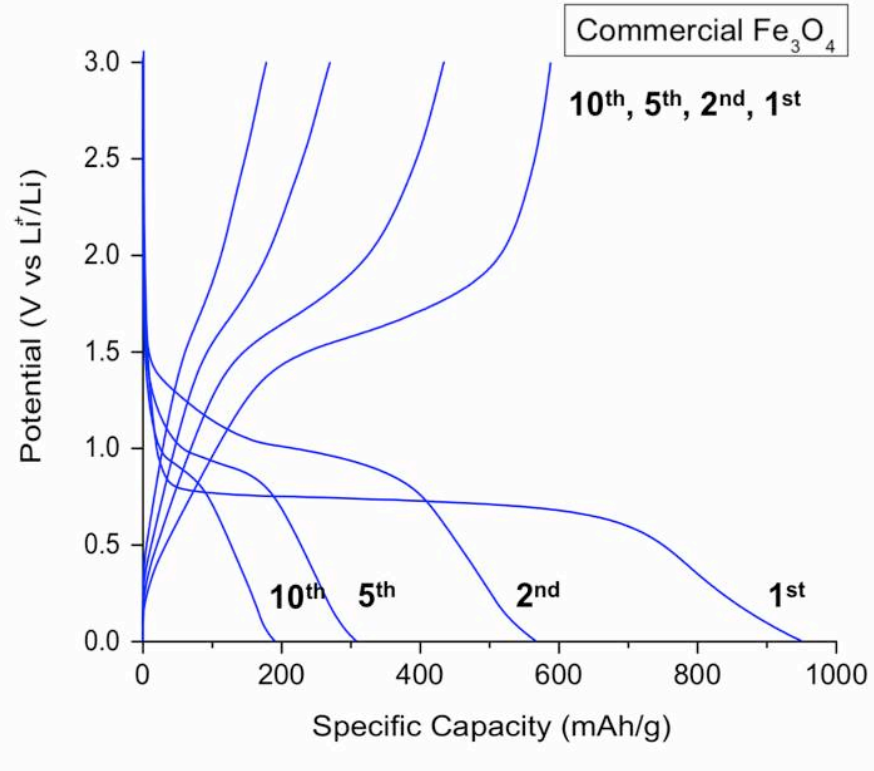

Figure 44: The charge and discharge curves of commercial Fe_3O_4 for 1st, 2nd, 5th and 10th cycle at 200 mA/g.

In addition, the commercial Fe_3O_4 was prepared in a slurry cast method to compare with the binder-free method. The Fe_3O_4 was mixed with carbon black and binder according to 8:1:1 wt. ratio and casted onto a Cu foil as current collector. The specific capacities for commercial Fe_3O_4 at 2nd, 5th, and 10th cycles fade faster than film

(Figure 44). This volume change (~ 50 %) occurred from Fe_3O_4 to Fe leads to fading specific capacity during charge/discharge process. In addition, Fe_3O_4/Fe/LiO_2 has low electrical conductivity. The interconnected conductive carbon black network easily breaks when volume changes of Fe_3O_4 nanocrystals occur. The Fe_3O_4 was left alone in the electrode when disconnected to conductive carbon black. The efficient lithium ion shuttling process between working and counter/reference electrode is hindered. As a result, the cyclic performance of commercial Fe_3O_4 fades quickly.

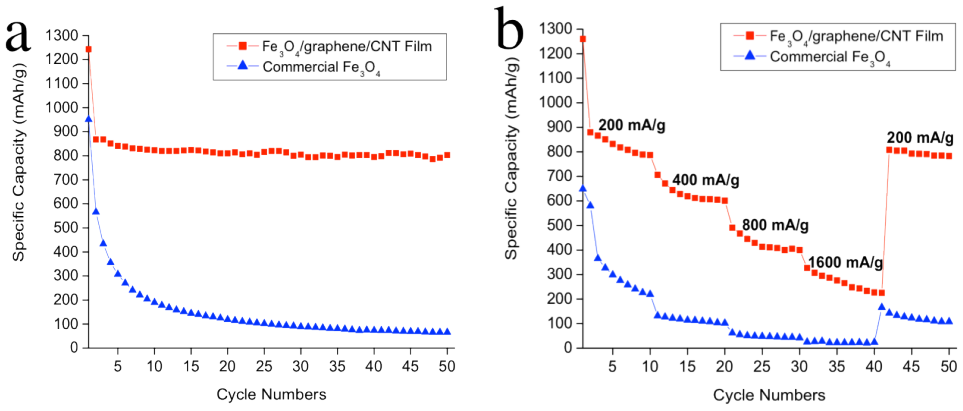

Figure 45: (a) Cyclic performance of Fe_3O_4/graphene/CNT film (red square) and commercial Fe_3O_4 (blue triangle) at 200 mA/g. (b) Rate capability of Fe_3O_4/graphene/CNTs film (red square) in comparison to commercial Fe_3O_4 (blue triangle).

The cyclic performance of Fe_3O_4/graphene/CNT film has much higher specific capacities than commercial Fe_3O_4. The reason is binder-free film provide interconnected electronic network, thus, the electrochemical reactions smoothly proceed in both directions. However, the commercial Fe_3O_4 prepared in slurry-cast method has limited electronic pathway because the carbon black particles cannot wrap and cover the Fe_3O_4

entirely. Upon cycling, the volume change of iron oxides also lead to failure of continuous electronic contact. Therefore the amount of available of iron oxides is limited. Figure 45a compares the cyclic performance of Fe_3O_4/graphene/CNT film with commercial Fe_3O_4. The film's 10^{th}, 20^{th}, and 30^{th} specific capacities are 823, 810, and 805 respectively. The specific capacity of film stabilized at 803 mAh/g in comparison to 90 mAh/g for commercial Fe_3O_4 at the end of 50 cycles. Moreover, rate capability was studied to compare the performances under different current density. The higher current density means the faster electrochemical reaction rate. Figure 45b compares the rate capability of Fe_3O_4/graphene/CNT film with commercial Fe_3O_4. The film delivered specific capacities of 787, 601,400, 225 and 783 mAh/g at 200, 400, 800, 1600, and 200 mA/g. The specific capacity of film at higher current density is more than 5 folds higher than that of commercial Fe_3O_4. For Fe_3O_4/graphene/CNT film, graphene sheet serves as an effective buffering to accommodate the metal oxide volume change of during the cycling.[65] CNTs provide robust conductive structure and fast electron transmission rate between metal oxide loaded graphene sheets, even at high current densities. Both graphene sheets and CNTs further improve the electronic conductivity of the iron oxides. The specific capacity of this film is much higher than that of each component alone. This binder-free method also reduced the electrode weight by eliminating the extra 200% wt. from Cu foil as current collector. The synergistic effect from CNTs,

graphene and Fe_3O_4 demonstrated excellent stability and high specific capacity retention, which are not available for Fe_3O_4 prepared in slurry-cast method.

2.4 Conclusions

In summary, we prepared the freestanding, flexible and conductive Fe_3O_4/graphene/CNT film as lithium ion battery anodes. The lightweight conductive films were tested as LIB anodes without binder and metal current collector. It showed stable and reversible a specific capacity of 805 mAh/g at 200 mA/g in 50 cycles. The effects of annealing process and carbon ratio on the overall electrode performances were studied. Due to the synergistic effect of graphene, CNT and iron oxides, the composite film has the advantages in terms of lithium ion storage capacity, rate capability, and cyclic stability.

3. Facile Synthesis of Three-dimensional Metal Oxide/Carbon co-Aerogel Nanostructures and Their Application for Energy Storage

3.1 Introduction

Energy storage is an important component for future renewable energy applications. Generally, batteries, electrochemical capacitors (ECs), and fuel cells are the three main electrochemical systems used in energy storage.[1]

According to a recent review on energy storage, 2-D electrochemical cells are fundamentally limited in the amount of energy that they can store per unit area, mass, and volume.[93] The ideal electrodes would contain a 3-D interpenetrating network of electron and ion pathways, which could offer major gains in energy and power density.[9,61] Carbon aerogel, a novel 3-D nanostructured electrode material, has many interesting properties, such as ultra lightweight, aperiodic continuous porosities (> 80 %), high surface areas (400-1200 m^2/g), and good electrical conductivity.

Nanoscale electrode materials have advantages including fast lithium insertion/extraction, large specific surface area and shortened Li^+ transport distance. [94,95] One of the challenges for nanostructured electrodes is to obtain a high volume fraction of electrochemically active nanostructured material and efficient ion/electron pathway at the same time.[96] Traditional graphite-based anodes for LIBs have disadvantages such as high irreversible capacity loss in the first cycle, and poor performance under high

charge/discharge rates.[13] Nanosize TiO_2 anode materials are a promising alternative to carbonaceous ones in terms of safety, relatively high lithium insertion voltage, and shortened lithium ion transport distance. [97,98] Chen *et al.* reported facile synthesis of 3-D hierarchical anatase phase TiO_2 spheres with a reversible capacity of 174 mA h/g after more than 100 charge-discharge cycles at 1 C.[14] These sphere surfaces were composed of ultrathin and large TiO_2 nanosheets with nearly 100% exposed (001) facets, which lead to fast lithium ion insertion/desertion process and the high Brunauer-Emmett-Teller (BET) surface area around 170 m^2/g. Rohlfing *et al.* prepared highly organized mesoporous TiO_2 films template from different amphiphilic block copolymers.[99] Large amounts of charge (ca. 200–250 mA h/g) were reversibly stored in the KLE / TiO_2 films possessing 3D cubic mesoporous structure. Kubiak *et al.* studied the electrochemistry performance of anatase TiO_2 nanoparticle networks with various BET surface areas (range from 25 to 150 m^2/g) and pore size distributions.[13] The TiO_2 nanoparticle (pore diameter 6 nm, crystallite size 9 nm, BET surface area 110 m^2/g) showed capacities of 160, 144, and 133 mAh/g at 1 to 3 C cycling rate.

Here, we presented a facile sol-gel approach to synthesize a well-connected conductive 3-D TiO_2/carbon aerogel nanocomposite structure and studied their lithium insertion performances. Our goal is to prepare 3-D nanostructured electrode material with interpenetrating electrochemical active metal oxide and carbon framework in order

to improve the LIB performance in terms of capacities, fast lithium ion insertion rates, and high BET surface area.

3.2 Experimental sections

3.2.1 Carbon aerogel synthesis

1.00 g resorcinol was dissolved in 47.1 g water in a glass vial. Then 1.47 g formaldehyde and 2.41 g catalyst solution (0.20 g Na_2CO_3 dissolved in 100 g water) were added. Seal the vial and stir the mixtures for 24 hours with a magnetic bar. The solution was cured in an oven for 3 days at 70 °C. Then the gel was soaked in acetone for 2 days. The solvent was changed 3 times in the first day. Next, CO_2 critical point drying (CPD) was used to remove the water in the gel. The dried RF aerogel was collected in a crucible, which was put in the hot zone of a chemical-vapor deposition furnace under argon (Ar) at the flow rate 300 cm^3/min. The temperature was raised from 25 to 900 °C in 1 hour, and then maintained at 900 °C for 4 hours and finally cooled down to room temperature.

3.2.2 C/TiO_2 co-aerogel aerogel synthesis

3.2.2.1 Preparation of resorcinol-formaldehyde (RF) sol precursor

1.0 g Resorcinol (R), 1.48 g formaldehyde (F) and 0.006 g sodium bicarbonate in 8.0 g ethanol (E) were mixed in a glass vial. The molar ratio of R/E, R/F and R/S were 0.0524, 0.5 and 200 individually. A 10-min bath sonication was used to obtain a homogeneous transparent solution.

3.2.2.2 Preparation of TiO_2 (Ti) sol precursor

2.84 g titanium (IV) isopropoxide (Ti) and 9.22 g ethanol were added in the other glass vial at room temperature and the molar ratio of Ti/E was 0.05. Take another a 30 ml glass vial, 5 ml of the RF sol precursor and 1.45g HCl (1.5M) were added. Then another pre-prepared 5ml Ti sol precursor was added, and followed by a 3-min bath sonication. After 30 minutes, this transparent solution became gel. Then, the sealed the vial and was heated in an oven at 75°C for 3 days as aging process for the TiO_2/RF co-aerogel. Subsequently, the organic/inorganic co-aerogel was dried via CO_2 CPD method. The co-aerogel samples were collected in a crucible, which was put in the hot zone of a chemical-vapor deposition furnace under argon (Ar) at the flow rate 800 cm^3/min. The temperature was raised from 25 to 900 °C in 1 hour, and then maintained at 900 °C for 4 hours and cooled down to room temperature.

3.2.3 Preparation of LIB electrodes

A two-electrode Swagelok-type cell was assembled in a glove box. A small piece of TiO_2/carbon (TiO_2:RF-1:1) co-aerogel monolith (~ 0.9 mg) was tested as a working electrode. Lithium foils served as the counter electrode and reference electrode. The electrolyte contained 1 M of $LiPF_6$ in the mixture of ethylene carbonate (EC), dimethyl carbonate (DMC) and diethyl carbonate (DEC) in 1:1:1 w/w ratio. The cells were cycled by a galvanostatic charge/discharge procedure. The voltage ranges we used were 0.05–3

V and 1-3 V vs. Li/Li^+. A carbon aerogel monolith prepared at the same pH value was used as the electrode in a control experiment.

3.3 Results and discussion

Both TiO_2 sol and RF sol were separately prepared and then mixed together according to different ratio (Figure 46a). Here these samples are denoted according to the precursor sol volume ratio, such as TiO_2:RF-1:1. Co-aerogels were prepared with different RF sol: TiO_2 sol ratio. Then 1.5 M HCl was added dropwise to adjust the pH value around 1.3. Afterward the glass vial was sealed air tight to avoid ethanol evaporation and cured in an oven for 5-days at 72 °C (Figure 46b). The TiO_2/organic RF co-aerogel was further soaked in acetone for a 5-hour solvent exchange to remove the small amount of water (Figure 46c). After critical point drying and pyrolysis, the TiO_2/organic RF co-aerogel converted to TiO_2/carbon co-aerogel (Figure 46d). The monolith shape was well maintained.

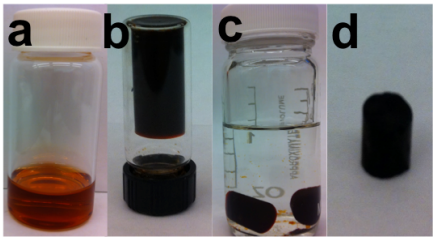

Figure 46: Optical photos showing a mixture of TiO_2 and RF sol (a), TiO_2/RF organic co-aerogel after 5-day aging under 72 °C in oven (b), solvent exchange in acetone(c), and TiO_2/carbon co-aerogel monolith after 4-hour pyrolysis under 900 °C in nitrogen atmosphere (d).

After 1-day magnetic stirring at room temperature in an airtight glass bottle, resorcinol-formaldehyde (RF) solution changed from transparent colorless to transparent brown, which indicated the initiation reaction between the resorcinol and formaldehyde precursors at the presence of catalyst Na_2CO_3. The solution was heated at 72 °C in an oven for 1-day, forming a gel-like morphology. Then Acetic acid (15 wt.%) solution was added to increase the mechanical stability.[100] Another 5 days of heating under 72 °C was usually required for further aging process. Next, the gel was washed with acetone repeatedly to exchange the water inside the RF organic aerogel. The critical point drying (CPD) dried the RF organic aerogel by exchanging the acetone with liquid CO_2 and drying the aerogel around 40 °C. Here, organic solvent washing before CPD was important because water from the original RF organic aerogel was immiscible with liquid CO_2. Figure 47 shows the RF organic aerogel before and after CPD treatment. The shrinking was attributed to incomplete solvent exchange between acetone and liquid CO_2. Finally the dried RF organic aerogel was converted to conductive carbon aerogel via 900 °C pyrolysis in N_2 atmosphere for 4 hours. The BET surface area of the carbon aerogel was 896 m^2/g.

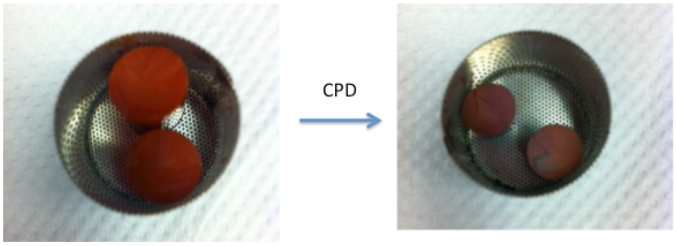

Figure 47: Optical photo showing organic RF aerogel before and after critical point drying.

For TiO_2-RF co-aerogel preparation method, both TiO_2 sol and RF sol were prepared in two glass vials and then mixed together according to different precursor ratio denoted as TiO_2:RF-1:1. Here, ethanol was used as solvent instead of water because TiO_2 precursor titanium isopropoxide was sensitive to H_2O. As a result, the acetone solvent exchange time was greatly reduced because ethanol is an organic solvent and could easily exchange with liquid CO_2 during CPD. We also chose acidic condition to stabilize the sensitive titanium isopropoxide and reduce the RF aerogel gelation time. Other procedures, such as heating in an oven, CPD, and calcination process were similar to that of the carbon aerogel mentioned above.

Figure 48a shows a piece of TiO_2-carbon co-aerogel (TiO_2:RF-1:1) monolith. SEM image shows it has a rough and porous surface (Figure 48d); BET surface area was around 437 m^2/g. After removing carbon by heating the co-aerogel in air at 500 °C, the TiO_2 materials still formed a three-dimensional interconnected framework with a BET SA around 11 m^2/g (Figure 48a, Figure 48c). Similarly, when the TiO_2 was removed with HF etching, the carbon materials kept the monolith morphology with a BET SA around

915 m^2/g (Figure 48b). We believe the TiO_2-carbon co-aerogel is composed of randomly interconnected TiO_2 and carbon framework (Figure 48g).

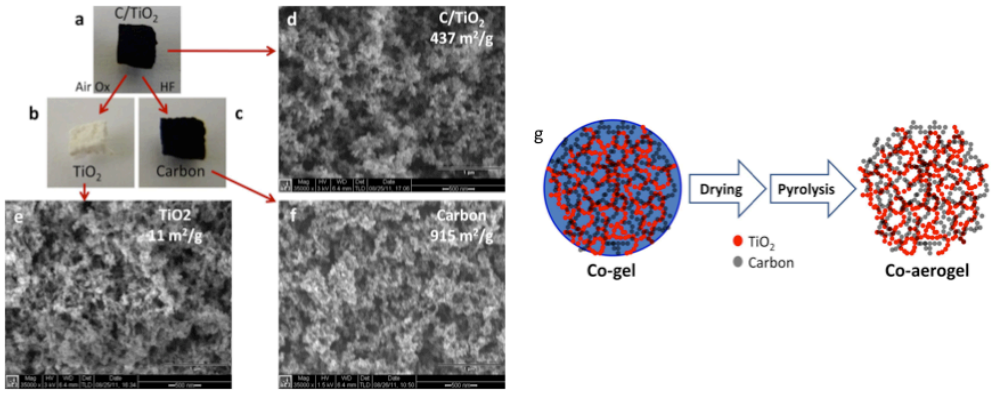

Figure 48: Optical images showing a piece of TiO_2/carbon co-aerogel monolith (a), TiO_2 aerogel after removing carbon component by air oxidation at 500°C for 5 hours (b), carbon aerogel after removing TiO_2 component by HF treatment for 24 hours(c), and respective SEM pictures (d-f). The proposed co-aerogel structure scheme (g). SEM images contributed by our previous group memeber Dr. Sungwoo-Yang.

High magnification TEM image demonstrates the interconnected TiO_2 crystals were wrapped by carbon aerogel (Figure 49a, Figure 49b). XRD pattern of the co-aerogel shows the anatase phase TiO_2 (Figure 49c). Figure 49d illustrates the specific surface area of the co-aerogel can be tuned by controlling TiO_2 ratio in co-aerogel. In addition, thermal gravimetric analysis (TGA) shows that the co-aerogel has 58 wt.% of TiO_2.

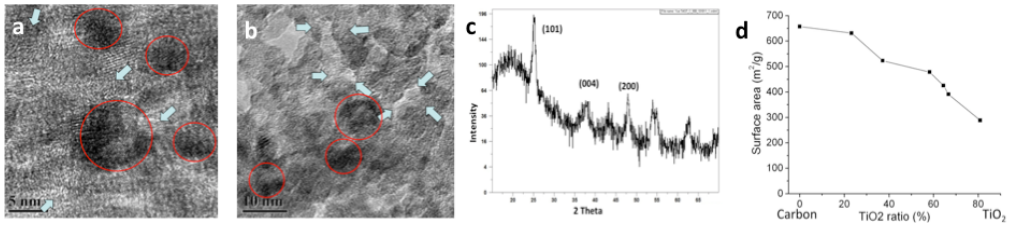

Figure 49: High magnification TEM images showing TiO_2 nanocrystals well mixed in carbon matrix (a, and b), the blue arrows marked the carbon layers, and the red circles marked the TiO_2 particles. XRD patterns of anatase phase TiO_2 in the co-

aerogel (c). BET surface area of TiO_2-carbon co-aerogel samples with different TiO_2 ratio (d). TEM images contributed by our collaborator Dr. Haiyan Wang.

The electrochemical performance of the TiO_2-carbon co-aerogel (TiO_2:RF-1:1) was measured by galvanostatic cycling between 0.05–3 V and 1-3 V vs. Li/Li^+. Generally, 1-3 V vs. Li^+/Li window is used for pure TiO_2 based electrode material. Regarding the TGA result, this co-aerogel contained 58 % wt. TiO_2. The role of carbon was not negligible in specific capacity. Therefore we adopted the 0.05-3 V vs Li^+/Li window. The Li^+ insertion/extraction reaction with TiO_2 occurs according to this reaction at 1.4-1.8 V vs. Li/Li^+:

$$x\ Li^+ + TiO_2 + x\ e^- = Li_xTiO_2$$

The theoretical specific capacity is 335 mAh/g, when x=1. Here, we define the scan rate 1C =168 mA/g based on the most consistently reported max insertion of Li of anatase phase TiO_2: x= 0.5 (168 mA/g).[101] Lithium foil was used as reference electrode because it a stable electrode potential, and the electrolyte was very sensitive to oxygen and water. Therefore, traditional reference electrodes such as Ag/AgCl electrode did not match this requirement.

Between 0.05-3 V vs. Li^+/Li at 1 C, the TiO_2-carbon (TiO_2:RF-1:1) co-aerogel first discharge specific capacity was 648.7 mAh/g (Figure 50a), which was higher than that of the reference carbon electrode (214.9 mAh/g) (Figure 50b). The plateau at 1.75 V indicated the lithium insertion of the anatase phase TiO_2. After 10 cycles, discharge specific capacities for co-aerogel and the carbon aerogel were 466.7 mAh/g and 106.6

mAh/g. The irreversible losses were 28.1% and 50.4%, respectively. Generally, the value 30% -45% is normal for TiO_2 based material after the first cycle.[66] The specific capacity was comparable to reported values under same window at 1 C. For instance, carbon nanotube coated with TiO_2 nanosheets with 320 mAh/g[66]. Between 1-3 V vs. Li^+/Li at 1 C, the TiO_2-carbon co-aerogel showed a specific capacity of 203.9 mAh/g in the first cycle (Figure 50d). The value was higher than the theoretical value of 168 mAh/g for TiO2 materials, indicating high insertion co-efficient for the first cycle. This phenomenon could be attributed to abundance surface active sites for lithium insertion.[14]

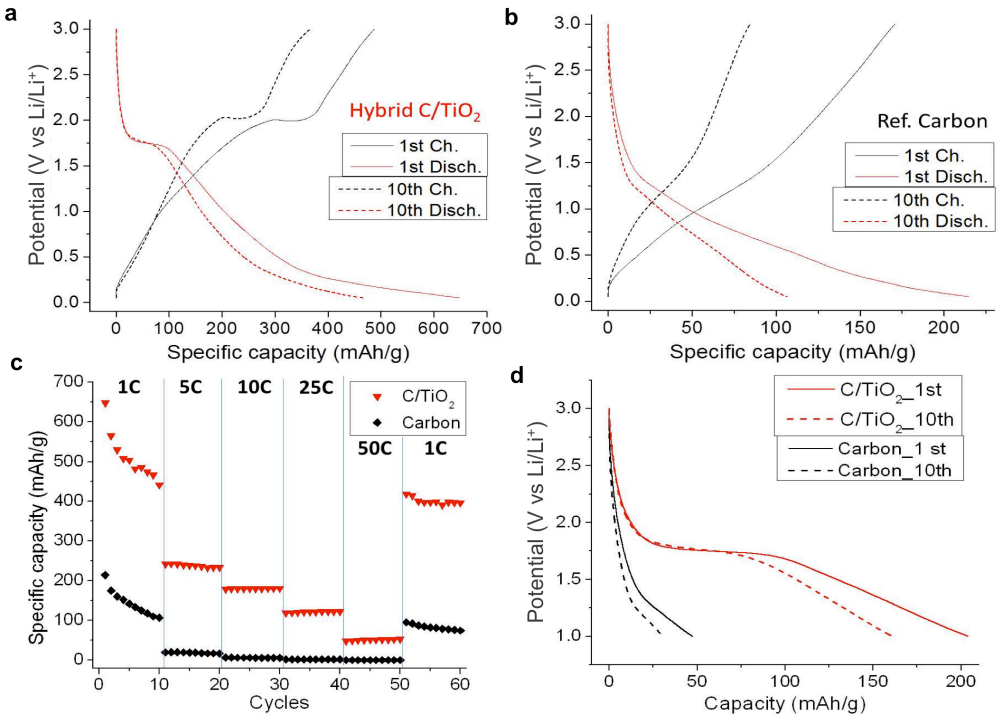

Figure 50: The 1st and 10th galvanostatic charge and discharge curves of the TiO_2/carbon co-aerogel (a) and reference carbon aerogel (b) at a rate of 1C (= 168 mA/g) in 0.05-3.0 V vs. Li^+/Li window. Scan rate performance (from 1C to 50C, then back to

1C) for co-aerogel in comparison to carbon aerogel (c). The 1st and 10th galvanostatic charge and discharge curves of the TiO_2/carbon co-aerogel (d) in 1.0-3.0 V vs. Li^+/Li window.

The rate capabilities of TiO_2-carbon co-aerogel at charging rages ranging from 1 to 50 C between 0.05-3 V vs. Li^+/Li are shown in (Figure 50c). Notably, when the current rate is reduced back to 1C at 60 cycles, the reversible discharge capacity was stabilized at ~400 mAh/g. This superior performance can be attributed to (1) High surface area of the TiO_2/carbon_1:1 co-aerogel monolith, which favors lithium ion insertion. (2) The carbon aerogel has a monolith shape, which provides strong mechanical stability even after high temperature treatment. Unlike traditional electrode preparation method, which requires 70 wt.% active material powders, 20 wt.% conductive carbon black and 10 wt.% binder (e.g. PVDF) to prepare the electrode, the conductive co-aerogel monolith are free of carbon additives and binder. (3) Finally, 3-D porous structure with conductive carbon skeleton favors lithium ion insertion.

3.4 Conclusions

In summary, we successfully prepared RF organic aerogel and converted it to 3-D aperiodic carbon aerogel via sol-gel method, solvent exchange, critical point drying, and high temperature pyrolysis. We also introduced metal oxide into this system, forming a monolith TiO_2/carbon co-aerogel even without carbon additives (increasing conductivity) and binder. The monolith morphology was well maintained even after high temperature heating. This new material is composed of interconnected anatase

phase TiO_2 and carbon aerogel 3-D network, providing high surface area (437 m^2/g), and a specific capacity at ~400 mAh/g at 168 mA/g current density during 60 cycles.

Appendix A

Publications:

1. Monolithic co-Aerogels of Carbon/Titanium Dioxide as Three Dimensional Nanostructured Electrodes for Energy Storage, Sungwoo Yang, **Yue Cai**, Yingwen Cheng, Chakrapani V. Varanasi and Jie Liu, *Journal of Power Sources*, **2012**, doi: 10.1016/j.jpowsour.2012.06.070.

2. Free-standing and Highly Conductive Fe3O4/Graphene/CNT Film as Anode for Lithium-Ion Batteries, **Yue Cai**, Yingwen Cheng, Songtao Lu, Hongbo Zhang, C. V. Varanasi and Jie Liu, to be submitted to Nanoscale

Conference Presentation:

1. Optimization of Metal oxide/Carbon Co-aerogel Material Properties and Application for Energy Storage, **Yue Cai**, Sungwoo Yang, Yingwen Cheng, Chakrapani V. Varanasi and Jie Liu, Materials Research Society (MRS) 2012 - Spring International Symposium, Moscone West Convention Center - San Francisco, California, April 13, 2012

Conference Posters:

1. Free-standing Conductive Fe_3O_4/Graphene/CNT Film As Anodes for Lithium-Ion Batteries, **Yue Cai**, Yingwen Cheng, Songtao Lu, Hongbo Zhang, C. V. Varanasi and Jie Liu, American Physical Society (APS) 2013-March Meeting, Baltimore, Maryland, March 21, 2013

2. Free-standing Conductive Fe_3O_4/Graphene/CNT Film As Anodes for Lithium-Ion Batteries, **Yue Cai**, Yingwen Cheng, Songtao Lu, Hongbo Zhang, C. V. Varanasi and Jie Liu, Materials Research Society (MRS) 2013 - Spring International Symposium, Moscone West Convention Center - San Francisco, California, April 4, 2013

References

1. Winter, M. & Brodd, R. J. What Are Batteries, Fuel Cells, and Supercapacitors? *Chem. Rev.* **104**, 4245–4270 (2004).

2. Cheng, F., Liang, J., Tao, Z. & Chen, J. Functional Materials for Rechargeable Batteries. *Adv. Mater.* **23**, 1695–1715 (2011).

3. Sides, C. R., Li, N., Patrissi, C. J., Scrosati, B. & Martin, C. R. Nanoscale materials for lithium-ion batteries. *MRS Bull.* **27**, 604–607 (2002).

4. Choi, N.-S. *et al.* Challenges Facing Lithium Batteries and Electrical Double-Layer Capacitors. *Angew. Chem. Int. Ed.* **51**, 9994–10024 (2012).

5. Simon, P. & Gogotsi, Y. Materials for electrochemical capacitors. *Nat Mater* **7**, 845–854 (2008).

6. Rolison, D. R. & Nazar, L. F. Electrochemical energy storage to power the 21st century. *MRS Bull.* **36**, 486–493 (2011).

7. Patil, A. *et al.* Issue and challenges facing rechargeable thin film lithium batteries. *Materials Research Bulletin* **43**, 1913–1942 (2008).

8. Palacín, M. R. Recent advances in rechargeable battery materials: a chemist's perspective. *Chem. Soc. Rev.* **38**, 2565 (2009).

9. Liu, R., Duay, J. & Lee, S. B. Heterogeneous nanostructured electrode materials for electrochemical energy storage. *Chem. Commun.* **47**, 1384 (2011).

10. Chan, C. K. *et al.* High-performance lithium battery anodes using silicon nanowires. *Nature Nanotechnology* **3**, 31–35 (2007).

11. Esmanski, A. & Ozin, G. A. Silicon Inverse-Opal-Based Macroporous Materials as Negative Electrodes for Lithium Ion Batteries. *Adv. Funct. Mater.* **19**, 1999–2010 (2009).

12. Liu, J. & Liu, X.-W. Two-Dimensional Nanoarchitectures for Lithium Storage. *Adv. Mater.* **24**, 4097–4111 (2012).

13. Kubiak, P. *et al.* TiO2 Anatase Nanoparticle Networks: Synthesis, Structure, and Electrochemical Performance. *Small* **7**, 1690–1696 (2011).

14. Chen, J. S. *et al.* Constructing Hierarchical Spheres from Large Ultrathin Anatase TiO 2Nanosheets with Nearly 100% Exposed (001) Facets for Fast Reversible Lithium Storage. *J. Am. Chem. Soc.* **132**, 6124–6130 (2010).

15. ZHOU, X., Wan, L. J. & Guo, Y. G. Binding SnO2 Nanocrystals in Nitrogen-Doped Graphene Sheets as Anode Materials for Lithium-Ion Batteries. *Adv. Mater.* (2013).

16. Lou, X. W., Deng, D., Lee, J. Y. & Archer, L. A. Preparation of SnO 2/Carbon Composite Hollow Spheres and Their Lithium Storage Properties. *Chem. Mater.* **20**, 6562–6566 (2008).

17. Tartaj, P., Morales, M. P., Gonzalez-Carreño, T., Veintemillas-Verdaguer, S. & Serna, C. J. The Iron Oxides Strike Back: From Biomedical Applications to Energy Storage Devices and Photoelectrochemical Water Splitting. *Adv. Mater.* **23**, 5243–5249 (2011).

18. Rao, C. N. R., Sood, A. K., Subrahmanyam, K. S. & Govindaraj, A. Graphene: The New Two-Dimensional Nanomaterial. *Angew. Chem. Int. Ed.* **48**, 7752–7777 (2009).

19. Geim, A. K. Graphene: Status and Prospects. *Science* **324**, 1530–1534 (2009).

20. Allen, M. J., Tung, V. C. & Kaner, R. B. Honeycomb Carbon: A Review of Graphene. *Chem. Rev.* **110**, 132–145 (2010).

21. Novoselov, K. S. Electric Field Effect in Atomically Thin Carbon Films. *Science* **306**, 666–669 (2004).

22. Chen, Z. Three-dimensional flexible and conductive interconnected graphene networks grown by chemical vapour deposition. *Nat Mater* **10**, 424–428 (2011).

23. Kim, K. S. *et al.* Large-scale pattern growth of graphene films for stretchable transparent electrodes. *Nature* (2009).

24. Geim, A. K. & Novoselov, K. S. The rise of graphene. *Nat Mater* **6**, 183–191 (2007).

25. Dikin, D. A. *et al.* Preparation and characterization of graphene oxide paper. *Nature* **448**, 457–460 (2007).

26. Park, S. & Ruoff, R. S. Chemical methods for the production of graphenes. *Nature Nanotechnology* **4**, 217–224 (2009).

27. Compton, O. C. & Nguyen, S. T. Graphene Oxide, Highly Reduced Graphene Oxide, and Graphene: Versatile Building Blocks for Carbon-Based Materials. *Small* **6**, 711–723 (2010).

28. Li, D., Müller, M. B., Gilje, S., Kaner, R. B. & Wallace, G. G. Processable aqueous dispersions of graphene nanosheets. *Nature Nanotechnology* **3**, 101–105 (2008).

29. Stankovich, S. *et al.* Graphene-based composite materials. *Nature* **442**, 282–286 (2006).

30. Huang, X. *et al.* Graphene-Based Materials: Synthesis, Characterization, Properties, and Applications. *Small* **7**, 1876–1902 (2011).

31. Shin, M. K. *et al.* Synergistic toughening of composite fibres by self-alignment of reduced graphene oxide and carbon nanotubes. *Nature Communications* **3**, 650–8 (2012).

32. Yin, S., Niu, Z. & Chen, X. Assembly of Graphene Sheets into 3D Macroscopic Structures. *Small* **8**, 2458–2463 (2012).

33. Chen, W., Li, S., Chen, C. & Yan, L. Self-Assembly and Embedding of Nanoparticles by In Situ Reduced Graphene for Preparation of a 3D Graphene/Nanoparticle Aerogel. *Adv. Mater.* **23**, 5679–5683 (2011).

34. Zhang, X., Wang, B., Sunarso, J., Liu, S. & Zhi, L. Graphene nanostructures toward clean energy technology applications. *WENE* **1**, 317–336 (2012).

35. Li, N., Liu, G., Zhen, C., LI, F. & Zhang, L. Battery Performance and Photocatalytic Activity of Mesoporous Anatase TiO2 Nanospheres/Graphene Composites by Template-Free Self-Assembly. *Advanced Functional …* (2011).

36. Zhou, G. *et al.* Graphene-Wrapped Fe 3O 4Anode Material with Improved Reversible Capacity and Cyclic Stability for Lithium Ion Batteries. *Chem. Mater.* **22**, 5306–5313 (2010).

37. Wang, H., Casalongue, H. S., Liang, Y. & Dai, H. Ni(OH) 2Nanoplates Grown on Graphene as Advanced Electrochemical Pseudocapacitor Materials. *J. Am. Chem. Soc.* **132**, 7472–7477 (2010).

38. Wu, Z.-S. *et al.* Graphene Anchored with Co 3O 4Nanoparticles as Anode of Lithium Ion Batteries with Enhanced Reversible Capacity and Cyclic Performance. *ACS Nano* **4**, 3187–3194 (2010).

39. Liang, Y. *et al.* Co3O4 nanocrystals on graphene as a synergistic catalyst for oxygen reduction reaction. *Nat Mater* (2011).

40. Yu, G. *et al.* Enhancing the Supercapacitor Performance of Graphene/MnO 2Nanostructured Electrodes by Conductive Wrapping. *Nano Lett.* **11**, 4438–4442 (2011).

41. Paek, S. M., Yoo, E. J. & Honma, I. Enhanced cyclic performance and lithium storage capacity of SnO2/graphene nanoporous electrodes with three-dimensionally delaminated flexible structure. *Nano Lett.* (2008).

42. Wu, Z. S., Wang, D. W., Ren, W. & Zhao, J. Anchoring Hydrous RuO2 on Graphene Sheets for High-Performance Electrochemical Capacitors. *Advanced Functional …* (2010).

43. Iijima, S. Helical microtubules of graphitic carbon. *Nature* **354**, 56–58 (1991).

44. Hu, L., Hecht, D. S. & Grüner, G. Carbon Nanotube Thin Films: Fabrication, Properties, and Applications. *Chem. Rev.* **110**, 5790–5844 (2010).

45. De Volder, M. F. L., Tawfick, S. H., Baughman, R. H. & Hart, A. J. Carbon Nanotubes: Present and Future Commercial Applications. *Science* **339**, 535–539 (2013).

46. Kumar, N. A. *et al.* Highly Conducting and Flexible Few-Walled Carbon Nanotube Thin Film. *ACS Nano* **5**, 2324–2331 (2011).

47. PEKALA, R. W. & KONG, F. M. A Synthetic Route to Organic Aerogels - Mechanism, Structure, and Properties. *J. Phys. Colloques* **24**, C4–33–C4–40 (1989).

48. Reuß, M. & Ratke, L. RF-aerogels catalysed by ammonium carbonate. *J Sol-Gel Sci Technol* **53**, 85–92 (2009).

49. Pierre, A. C. & Pajonk, G. M. Chemistry of Aerogels and Their Applications. *Chem. Rev.* **102**, 4243–4266 (2002).

50. Al-Muhtaseb, S. A. & Ritter, J. A. Preparation and Properties of Resorcinol-

Formaldehyde Organic and Carbon Gels. *Adv. Mater.* **15**, 101–114 (2003).

51. Kim, K. H., Oh, Y. & Islam, M. F. Graphene coating makes carbon nanotube aerogels superelastic and resistant to fatigue. *Nature Nanotechnology* **7**, 562–566 (2012).

52. Wu, X.-L. *et al.* Biomass-Derived Sponge-like Carbonaceous Hydrogels and Aerogels for Supercapacitors. *ACS Nano* **7**, 3589–3597 (2013).

53. Olsson, R. T. *et al.* Making flexible magnetic aerogels and stiff magnetic nanopaper using cellulose nanofibrils as templates. 1–5 (2010).doi:10.1038/nnano.2010.155

54. Wu, Z.-S. *et al.* 3D Nitrogen-Doped Graphene Aerogel-Supported Fe 3O 4Nanoparticles as Efficient Electrocatalysts for the Oxygen Reduction Reaction. *J. Am. Chem. Soc.* **134**, 9082–9085 (2012).

55. Xu, Z., Zhang, Y., Li, P. & Gao, C. Strong, Conductive, Lightweight, Neat Graphene Aerogel Fibers with Aligned Pores. *ACS Nano* **6**, 7103–7113 (2012).

56. Nardecchia, S., Carriazo, D., Ferrer, M. L., Gutiérrez, M. C. & del Monte, F. Three dimensional macroporous architectures and aerogels built of carbon nanotubes and/or graphene: synthesis and applications. *Chem. Soc. Rev.* **42**, 794 (2012).

57. ElKhatat, A. M. & Al-Muhtaseb, S. A. Advances in Tailoring Resorcinol-Formaldehyde Organic and Carbon Gels. *Adv. Mater.* **23**, 2887–2903 (2011).

58. Al-Muhtaseb, S. A. & Ritter, J. A. Preparation and properties of resorcinol–formaldehyde organic and carbon gels. *Adv. Mater.* **15**, 101–114 (2003).

59. Biener, J. *et al.* Advanced carbon aerogels for energy applications. *Energy Environ. Sci.* **4**, 656 (2011).

60. Sassin, M. B., Mansour, A. N., Pettigrew, K. A., Rolison, D. R. & Long, J. W. Electroless Deposition of Conformal Nanoscale Iron Oxide on Carbon Nanoarchitectures for Electrochemical Charge Storage. *ACS Nano* **4**, 4505–4514 (2010).

61. Long, J. W. & Rolison, D. R. Architectural Design, Interior Decoration, and Three-Dimensional Plumbing en Route to Multifunctional Nanoarchitectures.

Acc. Chem. Res. **40**, 854–862 (2007).

62. Sassin, M. B., Chervin, C. N., Rolison, D. R. & Long, J. W. Redox Deposition of Nanoscale Metal Oxides on Carbon for Next-Generation Electrochemical Capacitors. *Acc. Chem. Res.* 120301090912007 (2012).doi:10.1021/ar2002717

63. Zhang, W.-M., Wu, X.-L., Hu, J.-S., Guo, Y.-G. & Wan, L.-J. Carbon Coated Fe 3O 4Nanospindles as a Superior Anode Material for Lithium-Ion Batteries. *Adv. Funct. Mater.* **18**, 3941–3946 (2008).

64. Zhao, Y., Li, J., Wu, C., Ding, Y. & Guan, L. A Yolk-Shell Fe3O4@C Composite as an Anode Material for High-Rate Lithium Batteries. *ChemPlusChem* **77**, 748–751 (2012).

65. Su, Y. *et al.* Two-Dimensional Carbon-Coated Graphene/Metal Oxide Hybrids for Enhanced Lithium Storage. *ACS Nano* **6**, 8349–8356 (2012).

66. Ding, S., Chen, J. S. & David Lou, X. W. One-Dimensional Hierarchical Structures Composed of Novel Metal Oxide Nanosheets on a Carbon Nanotube Backbone and Their Lithium-Storage Properties. *Adv. Funct. Mater.* **21**, 4120–4125 (2011).

67. Cao, F.-F. *et al.* Symbiotic Coaxial Nanocables: Facile Synthesis and an Efficient and Elegant Morphological Solution to the Lithium Storage Problem. *Chem. Mater.* **22**, 1908–1914 (2010).

68. Wu, H. B., Chen, J. S., Hng, H. H. & Wen David Lou, X. Nanostructured metal oxide-based materials as advanced anodes for lithium-ion batteries. *Nanoscale* **4**, 2526 (2012).

69. Endo, M., Muramatsu, H., Hayashi, T., Kim, Y. A. & Terrones, M. Buckypaper from coaxial nanotubes. *Nature* (2005).

70. Jia, X. *et al.* Building Robust Architectures of Carbon and Metal Oxide Nanocrystals toward High-Performance Anodes for Lithium-Ion Batteries. *ACS Nano* **6**, 9911–9919 (2012).

71. Zhou, G. *et al.* A nanosized Fe2O3 decorated single-walled carbon nanotube membrane as a high-performance flexible anode for lithium ion batteries. *J. Mater. Chem.* **22**, 17942 (2012).

72. Ban, C. *et al.* Nanostructured Fe3O4/SWNT Electrode: Binder-Free and High-Rate Li-Ion Anode. *Adv. Mater.* **22**, E145–E149 (2010).

73. Wu, Y., Wei, Y., Wang, J., Jiang, K. & Fan, S. Conformal Fe 3O 4Sheath on Aligned Carbon Nanotube Scaffolds as High-Performance Anodes for Lithium Ion Batteries. *Nano Lett.* **13**, 818–823 (2013).

74. Cheng, Y., Lu, S., Zhang, H., Varanasi, C. V. & Liu, J. Synergistic Effects from Graphene and Carbon Nanotubes Enable Flexible and Robust Electrodes for High-Performance Supercapacitors. *Nano Lett.* **12**, 4206–4211 (2012).

75. Tarascon, J.-M. & Armand, M. Issues and challenges facing rechargeable lithium batteries. *Nature* **414**, 359–367 (2001).

76. Wu, M.-S., Ou, Y.-H. & Lin, Y.-P. Iron Oxide Nanosheets and Nanoparticles Synthesized by a Facile Single-Step Coprecipitation Method for Lithium-Ion Batteries. *J. Electrochem. Soc.* **158**, A231 (2011).

77. Xin, S., Guo, Y.-G. & Wan, L.-J. Nanocarbon Networks for Advanced Rechargeable Lithium Batteries. *Acc. Chem. Res.* **45**, 1759–1769 (2012).

78. Li, L. *et al.* Selected-Control Synthesis of Monodisperse Fe3O4@C Core-Shell Spheres, Chains, and Rings as High-Performance Anode Materials for Lithium-Ion Batteries. *Chem. Eur. J.* **18**, 11417–11422 (2012).

79. Kang, E. *et al.* Fe3O4 Nanoparticles Confined in Mesocellular Carbon Foam for High Performance Anode Materials for Lithium-Ion Batteries. *Adv. Funct. Mater.* **21**, 2430–2438 (2011).

80. Lei, C. *et al.* Dopamine as the coating agent and carbon precursor for the fabrication of N-doped carbon coated Fe3O4 composites as superior lithium ion anodes. *Nanoscale* **5**, 1168 (2013).

81. Su, D. S. & Schlögl, R. Nanostructured Carbon and Carbon Nanocomposites for Electrochemical Energy Storage Applications. *ChemSusChem* **3**, 136–168 (2010).

82. Eder, D. Carbon Nanotube–Inorganic Hybrids. *Chem. Rev.* **110**, 1348–1385 (2010).

83. Lee, S. W. *et al.* High-power lithium batteries from functionalized carbon-nanotube electrodes. *Nature Nanotechnology* **5**, 531–537 (2010).

84. Dai, L., Chang, D. W., Baek, J.-B. & Lu, W. Carbon Nanomaterials for Advanced Energy Conversion and Storage. *Small* **8**, 1130–1166 (2012).

85. Yu, S.-H. *et al.* Structure-Properties Relationship in Iron Oxide-Reduced Graphene Oxide Nanostructures for Li-Ion Batteries. *Adv. Funct. Mater.* n/a–n/a (2013).doi:10.1002/adfm.201300190

86. Wu, Y., Wei, Y., Wang, J., Jiang, K. & Fan, S. Conformal Fe 3O 4Sheath on Aligned Carbon Nanotube Scaffolds as High-Performance Anodes for Lithium Ion Batteries. *Nano Lett.* **13**, 818–823 (2013).

87. Zhou, K., Zhu, Y., Yang, X. & Li, C. One-pot preparation of graphene/Fe3O4 composites by a solvothermal reaction. *New J. Chem.* **34**, 2950 (2010).

88. Qian, C., Qi, H. & Liu, J. Effect of tungsten on the purification of few-walled carbon nanotubes synthesized by thermal chemical vapor deposition methods. *J. Phys. Chem. C* (2007).

89. Hou, Y. *et al.* Functionalized Few-Walled Carbon Nanotubes for Mechanical Reinforcement of Polymeric Composites. *ACS Nano* **3**, 1057–1062 (2009).

90. Zhu, X., Zhu, Y., Murali, S., Stoller, M. D. & Ruoff, R. S. Nanostructured Reduced Graphene Oxide/Fe 2O 3Composite As a High-Performance Anode Material for Lithium Ion Batteries. *ACS Nano* **5**, 3333–3338 (2011).

91. Whittingham, M. S. Lithium Batteries and Cathode Materials. *Chem. Rev.* **104**, 4271–4302 (2004).

92. Arora, P. & Zhang, Z. J. Battery Separators. *Chem. Rev.* **104**, 4419–4462 (2004).

93. Rolison, D. R. *et al.* Multifunctional 3D nanoarchitectures for energy storage and conversion. *Chem. Soc. Rev.* **38**, 226 (2008).

94. Bruce, P. G., Scrosati, B. & Tarascon, J.-M. Nanomaterials for Rechargeable Lithium Batteries. *Angew. Chem. Int. Ed.* **47**, 2930–2946 (2008).

95. Liu, J. *et al.* Oriented Nanostructures for Energy Conversion and Storage. *ChemSusChem* **1**, 676–697 (2008).

96. Aricò, A. S., Bruce, P., Scrosati, B., Tarascon, J.-M. & van Schalkwijk, W. Nanostructured materials for advanced energy conversion and storage devices.

Nat Mater **4**, 366–377 (2005).

97. Armstrong, A. R., Armstrong, G., Canales, J., Garc a, R. & Bruce, P. G. Lithium-Ion Intercalation into TiO2-B Nanowires. *Adv. Mater.* **17**, 862–865 (2005).

98. Sun, Z. *et al.* Rational Design of 3D Dendritic TiO 2Nanostructures with Favorable Architectures. *J. Am. Chem. Soc.* **133**, 19314–19317 (2011).

99. Fattakhova-Rohlfing, D., Wark, M., Brezesinski, T., Smarsly, B. M. & Rathouský, J. Highly Organized Mesoporous TiO2 Films with Controlled Crystallinity: A Li-Insertion Study. *Adv. Funct. Mater.* **17**, 123–132 (2007).

100. Despetis, F., Barral, K., Kocon, L. & Phalippou, J. Effect of Aging on Mechanical Properties of Resorcinol-Formaldehyde Gels. *J Sol-Gel Sci Technol* **19**, 829–831 (2000).

101. Yang, Z. *et al.* Nanostructures and lithium electrochemical reactivity of lithium titanites and titanium oxides: A review. *Journal of Power Sources* **192**, 588–598 (2009).